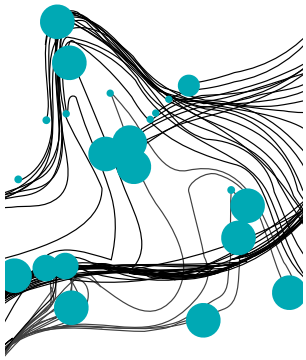

RAM ROBOTICS AND MECHATRONICS

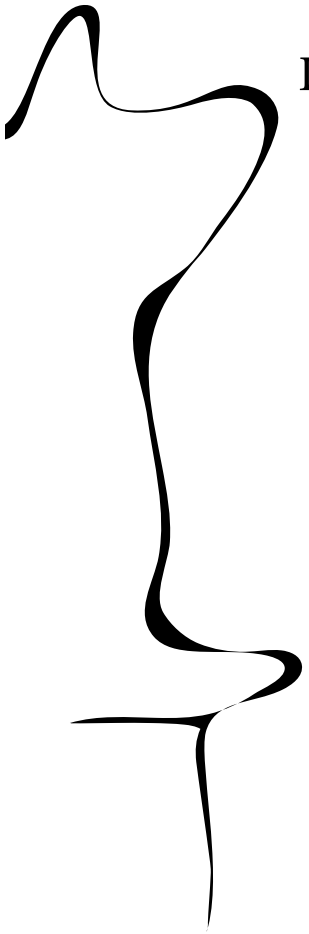

Deformation Prediction in Single-Segment Tendon-Driven Flexible Endoscope for Compensation of Gravity and External Loads Using Cosserat Rod Theory

W.B. (Willem) Hoitzing

MSC ASSIGNMENT

Committee:
prof. dr. ir. S. Stramigioli
dr. ir. M. Abayazid
Y.X. Mak, MSc
dr. ir. R.G.P.M. Aarts

June, 2020

019RaM2020
Robotics and Mechatronics
EEMCS
University of Twente
P.O. Box 217
7500 AE Enschede
The Netherlands

UNIVERSITY OF TWENTE. | TECHMED CENTRE

UNIVERSITY OF TWENTE. | DIGITAL SOCIETY INSTITUTE

Abstract

Flexible tendon-actuated endoscopes are used in minimally invasive surgery and can be robotically controlled to improve accuracy. Long and slender endoscopes are susceptible to external forces and moments, and for reliable control the deformation that is caused needs to be predicted and compensated for. A flexible tendon-actuated endoscopic system that can be robotically controlled while compensating for external load deformation was developed in this study. The designed actuation system shows successful basic functionality according to the design goal, with limitations regarding fine movements and tensioning of tendons. Additionally, control issues arise that call for control of each individual tendon's tension. Secondly, using a Cosserat based model, deformation prediction of external loads was experimentally validated by comparison to the physical case. Significant prediction errors are observed for model-based compensation, therefore it is chosen to instead perform additional model evaluations that hint towards significant friction in the tendons. In conclusion, the design and development oriented aspects of the thesis were successfully carried out for the most part, while deformation prediction and compensation first requires more insight into the friction during actuation.

Contents

1 Introduction

With new and advancing robotic technologies, applications to the medical field are examined and researched. Minimally invasive surgery (MIS) is an important trend the medical field has experienced. As an example, over 25 years ago (1992) the first video-assisted thoracoscopic surgery (VATS) anatomical lobectomy was performed [1], signifying the leap towards MIS in the treatment of early-stage lung cancer, as it is currently viewed a standard of care since the technique's safety and oncological effectiveness are widely established [2]. The first MIS procedure, however, was performed already in the early 19th century by the use of a cystoscope to look into and treat lesions in the bladder, avoiding a previously radical operation [3]. In 1931, Japanese orthopaedic surgeon Kenji Takagi published a case series on knee endoscopy using an arthoscope (a redesigned version of a cystoscope) [3, 4]. Subsequently in 1957, Marski Watanable (Takagi's pupil) published the *Atlas of Arthroscopy* based on extensive arthroscopy experience and further development of the device, which can be recognized as minimally invasive surgery's real introduction which has soon after become the focal point of new medical technology [3].

1.1 Minimally Invasive Surgery

Minimally invasive surgery — as the name would suggest — aims to reduce a procedure's body cavity invasion and inherent damage to the tissue by means of inserting specialized instrumentation through a limited number of small incisions, or even through natural orifices. MIS is beneficial to both the individual patient as well as society in general, as it may reduce patient discomfort, costs, hospital and recovery time, risk of infection, and may improve aesthetic outcome [5, 6]. Despite these advantages of MIS over traditional open surgery, the latter is not completely replaced. Open surgery may be necessitated by limited access to the point of interest, a patient's physical condition and/or their surgical history [6]. Depending on the area within the body that is operated on, and endoscopic intervention may be referred to with *laparoscopy* (abdominal or pelvic area) or *thoracoscopy* (organs of the chest), amongst others that are not specifically relevant to this thesis.

Recent advances further influence thoracic surgical approaches — which have already evolved from thoracotomy (open chest surgery) to minimally invasive endoscopic surgery such as VATS — driving them towards robotic-assisted thoracoscopic surgery, or RATS [7]. The Japanese national health insurance started to cover RATS for malignant lung tumours, and both benign and malignant mediastinal tumours since 2018, after already covering robot-assisted prostatectomy in 2012 [7]. This illustrates the more recent trend, advancing MIS by introducing robotic assistance. The new robotic technology can provide improved precision, intuitive ergonomic interfaces, and access to remote surgical sites through miniaturized instrumentation [5].

As the instrumentation is no longer directly manipulated by the surgeon's hand, but instead a robotic system is introduced, some safety issues arise. Force

feedback on the instrument's tip which is situated in the patient's tissue was previously directly felt by the surgeon through his manual manipulation of the tools. In the case of robotic manipulation, however, the surgeon loses this sense of touch and perception of the instrument's environment, also referred to as haptic feedback. It is reported that haptic feedback — especially feedback on the external forces the instrument is experiencing — is an important factor for improved patient safety in robotically operated interventional systems [8, 9]. For this reason an important aspect of surgical robotic systems is their integration of haptic feedback, typically requiring some effort regarding force sensing on the endoscope in the case of minimally invasive surgery.

Historically, endoscopes were rigid shafts optionally equipped with a bevelled tip for non-straight viewing angles (an oblique endoscope). Nowadays, flexible endoscopes are typically used for MIS [6, 10] providing the following advantages over traditional rigid endoscopes: tortuous paths (e.g. GI tract or cardiovascular canals) can be followed, the endoscope can be repositioned within the body and thus explore a wider range, and optional compliance can prevent rigid collisions with vital tissues or structures inside the body [10, 11]. Typical manually actuated flexible endoscopes are still quite limited in the sense that their workspace is confined, their visibility is limited, and dextrous tasks can only be performed by highly skilled endoscopists [12]. Dedicated robotic flexible manipulators are capable of more precisely controlling the tip's position and orientation, providing the sought-after distal tool-dexterity enhancement [8]. These manipulators should be scalable to small size, flexible yet strong, and have dextrous and agile movement for reaching surgical sites with traditionally difficult access in order to further advance MIS and overcome the current issues [5].

While an endoscope's dexterity, reachable workspace, and intrinsic safety for the patient may be improved by having a slender and flexible features, this may raise issues in controlling such an endoscope, whether it be manual or robotic. An endoscope's low stiffness and small diameter make it susceptible to external forces. Especially for long endoscopes (for example when multiple independently actuated segments are introduced), their movement may be significantly affected by gravity alone. In a clinical setting, a patient's internal organs will continuously deform an endoscope used during any intervention. To regain direct control over the deformed endoscope, the effect of external loads should be compensated for.

1.2 Aim

The aim of this thesis is to develop a flexible tendon-actuated endoscopic system, comprised of a single bending segment with two degrees of freedom, that can be robotically controlled while compensating for external load deformation. An additional aim for the design of the endoscopic system prototype is to allow extension in terms of control scheme by incorporating not only model-based load compensation but also teleoperation with integration of haptic feedback. By achieving this, it is hoped that the challenges faced in accurate robotic

control of slender flexible manipulators — that have been mentioned above — can be overcome. To help in achieving the aim, the following main research questions have been defined:

How accurately can a custom designed robotic actuation system predict and compensate for the effects of gravity and external loading on a slender single-segment tendon-actuated flexible manipulator?

Additionally, three supporting research questions are specified:

How should gravity/external load compensation be implemented?

How should a robotic flexible endoscopic system be designed to allow for external load compensation?

How well is endoscope deformation due to external loads (incl. gravity) predicted and compensated using the described model, in different endoscope configurations?

1.3 Research Plan

In order to answer the research questions, the following approach is taken. Firstly, recent literature is reviewed. Background on flexible endoscopes and their reported modelling approaches are investigated. The review will help to create an understanding of what path to take regarding the first supporting research question. Secondly, an actuation system is designed that should be able to steer an endoscope, incorporating compensation for external loads, while being flexible enough for the application of multiple control strategies, including the integration of haptic feedback. More specifically, the system's design requirements are identified, and the performance of the designed system, focussed on the most important design requirements, is experimentally evaluated. These results and their interpretation will answer the second supporting research question

Next, when the actuation system is designed and an approach to external load compensation has been identified, the chosen method is experimentally validated to evaluate its performance in the actuation system and answer the third supporting question. Finally, knowing the results of the specific approach that was chosen and the actuation system's performance, the main research question is discussed and answered.

1.3.1 Contribution and Novelty

It is intended that the research done in this thesis helps further improve patient outcome during clinical interventions requiring minimally invasive surgery. While the designed system serves as only a prototype, it resembles a step towards a new system with improved accuracy and dexterity compared to more traditional non-flexible endoscopes and manual control, through modelling external loads acting on the endoscope. The designed actuation system including

its external load compensation will serve as a novel approach for robotic endoscope control with model-based external load compensation.

1.4 Organisation

The current section of this thesis introduces the general context and goal of the thesis. Some background information is given to help define and motivate a problem statement in current clinical practice. The aim of the thesis is to contribute towards solving the identified problem, and several research questions are defined which structure an approach for the research that is done. The next section presents a literature review that has been conducted to investigate what other research has been done, and what is the current state of the art.

Following this section, the thesis is split into two main parts. In the first part, the focus is put on the design of the actuation system. The important design goals are identified in the first section under this part, and the final design is presented and motivated using some previous iterations and considerations in the next section.

The second part of the thesis draws the focus back on the compensation of external loads and especially the experimental validation of the system's performance. In two sections (Materials and Methods), the hardware and software used is listed, some relations between components of the system are highlighted, and the methods (including the experimental setup) are detailed. Then the results of the experiments and other methods with relevant outcomes are presented.

Subsequently, in the discussion section, results are interpreted, outliers are discussed, and recommendations for future research are given. From the discussion and further into the thesis, the scope includes both parts again, in order to arrive at a single evaluation of the entire system's applications and performance. Finally, in the section conclusion, the most important results and points of discussion are reflected on by drawing some conclusions. These conclusions are then related to the defined research questions and the aim of the thesis.

2 Literature Review

introduce the concept: explain/give typical or general approaches and conclude with recent advances. mention literature review on force sensing is omitted and presented in appendix

2.1 Flexible Robotic Endoscopes

Flexible robotic endoscopes are a type of flexible manipulators having the common application of assisting in or performing endoscopic surgery. Flexible manipulators are usually described to be continuum robots. A broad definition of a continuum robot is given by Burgner-Kahrs et al. [5]: *"A continuum robot is an actuatable structure whose constitutive material forms curves with continuous*

tangent vectors". Other definitions reported in the literature include terms such as "continuously bending", "infinite-DOF", "elastic structure", or "do not contain rigid links and identifiable rotational joints" [5]. Hyper-redundant robots — which attempt to approximate a continuum shape by serially connecting a high but finite number of discrete joints — are typically not considered continuum robots as they may only approximate the continuous tangent vector curves. However, it is a thin line between continuum and hyper-redundant robots that can be obscured by equipping continuously bending elastic elements with discrete joints to form one structure that is referred to by Burgner-Kahrs et al. [5] as pseudocontinuum robots. The so-called pseudocontinuum robots are included in this review as they may prove to be an interesting hybrid approach to flexible manipulators.

An important aspect of flexible manipulators is the method of actuation, which can be categorized into intrinsic and extrinsic actuation [5]. Intrinsically-actuated manipulators integrate the actuators inside the joints or endoscope backbone, whereas extrinsically-actuated manipulators rely on some form of mechanical transmission of externally generated forces to the endoscope structure. Typical intrinsic actuation methods include hydraulic/pneumatic chambers, shape memory effect, embedded micro-motors, fluidic fiber-reinforced elastomers, and McKibben muscles. Transmission methods for extrinsic actuation include tendon/cable driven mechanisms, multibackbone structures, and concentric-tube transmission by axial rotation and translation at the bases of layered tubes (see section 2.1.3 for more information about the concept of concentric tube manipulators). Extrinsic actuation is reported to be associated with reduced manipulator diameter, albeit at the cost of larger external footprint and increased friction and hysteresis when compared to intrinsic actuation methods. Because of the valuable down-scalability of extrinsically-actuated manipulators, the following sections are limited to flexible manipulators with extrinsic actuation.

Flexible manipulators may have different general structures [5]. Typical medical manipulators have one single elastic structure, placed centrally, which supports the passage of transmission elements and interventional tools. These manipulators are referred to as single backbone robots, whereas the other type is called a multi-backbone robot. Generally, the latter type is composed of parallel elastic rods or tubes, with some form of constrained dependencies. Backbones have been manufactured from a variety of materials such as springs, elastic rods or tubes (often a NiTi/nitinol alloy), moulded polymers, and in the case of robotic catheters also braided polymer tubes. Using slotting patterns along the length of the backbone, specific stiffness profiles of the backbone(s) can be obtained.

The choice in backbone has inherent limitations on the robot's range of motion and stiffness [5]. Strain during bending is proportional to the distance from the neutral axis of the backbone cross-section. As a result, small-diameter manipulators made of materials with high elastic limits can realize a larger range of motion, and thus are associated with a larger workspace within a patient. However, materials with high elastic strain limits typically have a relatively low

Young's modulus. In addition, as a manipulator's diameter is reduced, so is its moment of inertia of the cross-section. Both can significantly limit a manipulator's output stiffness, potentially preventing it from exerting the required tissue forces to perform an intervention. This means there is a typical design trade-off between workspace and stiffness. Nitinol backbone components are therefore widely used in surgical continuum robots, as this material has a high elastic stress limit (which is the product of Young's modulus and elastic strain limit). More financially-attractive alternatives are steels and carbon fiber composites, yet nitinol's biocompatibility and its availability of thin-walled tubes limits their popularity.

Recent reviews show that surgical flexible manipulators can be categorized into one of three prevailing designs [13]. These are: tendon-driven continuum manipulators, tendon-driven serpentine manipulators, and concentric tube manipulators. The three types of flexible manipulators will be discussed separately in the following subsections. As a general remark concerning the first two designs, it should be noted that tendon-driven mechanisms are associated with higher position accuracy, compared to a variety of other ex- and intrinsic actuation methods, including concentric tube manipulators [11].

2.1.1 Tendon-Driven Continuum Manipulators

The tendon-driven continuum manipulator (TCM) contains a continuum elastic backbone (or multiple) that bends according to the tension in a set of tendons. Figure 1 shows a two-segment TCM structure with the important components labelled. For planar manipulators, only two tendons per bending section or module are required. Two-dimensional bending segments typically use three coupled, or four (two independently actuated sets of two) tendons to be able to rotate around two axes. Spacer discs are rigidly connected to the backbone to transmit any exerted moments by tendon tension, and have holes to guide the tendons through. In the case of multi-segment manipulators, there are multiple sets of tendons that may need to act independent of each other. Therefore, the tendons associated with a distal module of the manipulator should be routed through the spacer discs of a proximal module according to a specific configuration as presented by Webster III and Jones [14] (see Fig. 2).

A *co-located* configuration may be the most straight-forward method as it simply routes proximal and distal tendons through the same holes, yielding some practical issues regarding increased friction and possibly other undesired behaviour stemming from tendon-tendon interactions. *Co-radially* configured spacer discs guide cables through holes that are positioned at equal angles from the central axis of the backbone. This configuration is scaleable, although it is spatially inefficient compared to the third option. This last configuration is referred to as the *distributed* tendon configuration, and it offsets sets of holes corresponding to independent modules by an angle relative to the backbone's neutral axis, keeping the distance from the centre equal. Although it may depend on the manipulator's cross-sectional diameter and the tendon's diameter, this latter configuration is arguably the most space-efficient solution to routing

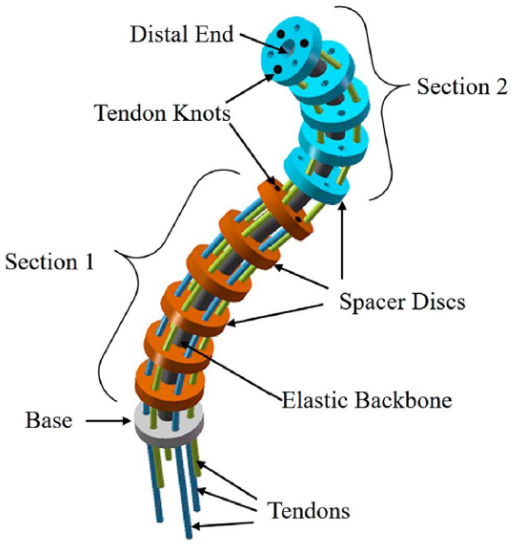

Figure 1: Illustration of structure and components tendon-driven continuum manipulator (using a distributed tendon configuration) [13].

tendons in multi-segment manipulators. As the number of modules increases further, the total number of tendons that the first proximal segment needs to guide will eventually get too large to distribute along a single circular profile; assuming the cross-sectional diameter doesn't increase irrationally to allow for more space. In this case, it is likely more efficient to use a combination of the co-radial and distributed approaches, starting a second ring around an initial ring of distributed tendon holes.

The tendon knots at the distal spacer disc of every module prohibit the tendon from slipping through when it is tensioned. Motors positioned below the manipulator's base may pull on one or multiple tendons — while loosening any antagonistic tendons — in order to actuate the manipulator. A tensioned tendon will pull on the distal spacer disc and thus exert a moment on the elastic backbone which will in result deform. When external forces and gravity are ignored this moment will ideally shape the backbone into a circular arc. This yields some useful modelling properties which will be discussed in the relevant section.

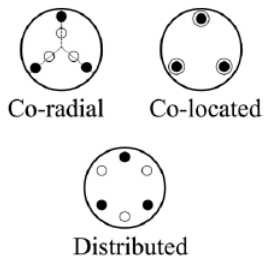

Figure 2: Different configurations of tendon routing holes in spacer discs, as presented in [14].

2.1.2 Tendon-Driven Serpentine Manipulators

Similar in structure to the TCM is the tendon-driven serpentine manipulator (TSM) design, which is shown in figure 3. It contains a flexible backbone and is typically actuated through transmission by tendons as well. It is not a continuum robot, however, as it uses a series of rigid joints that replace the spacer discs that are seen in the continuum design. The joints used can be revolute joints (for planar bending when they have parallel axes) or spherical joints (allowing free 2D rotation). The rigid joints are typically small and stacked closely together, leading to the frequent comparison to vertebrae.

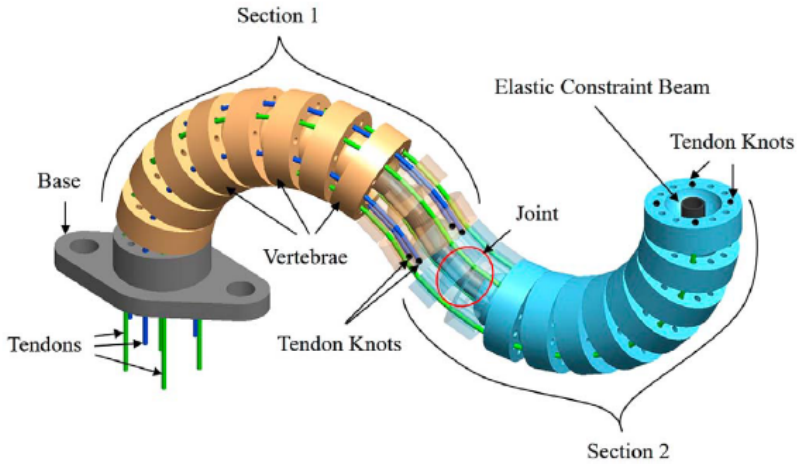

Figure 3: Illustration of structure and components tendon-driven serpentine manipulator (using a distributed tendon configuration) [13].

Since serpentine structures are extrinsically actuated through tendon transmission just like TCM designs, the general remarks about tendon routing mentioned in the subsection above translate directly. However, the ideal shape deformation due to a pulled tendon's moment — disregarding external loads and gravity — does not follow a circular arc. Due to the articulated coupling between the rigid links (which are 'free' spacer discs only rigidly connected through the elastic backbone in the case of TCM) a serpentine manipulator with n rigid links will bend as n faces of a regular polygon. When n approaches infinity, the serpentine segment will gradually transition into a continuously bending backbone and can therefore be classed as a TCM in the extreme case. It should also be noted that the usage of rigid joints typically comes at the costs of high friction (for revolute and spherical joints), or complex manufacturing (for flexure joints).

2.1.3 Concentric Tube Manipulators

The third design does not use tendon-based actuation, and is therefore fundamentally different from the previous two. Concentric tube manipulators (CTM) contain several nested pre-curved tubes (typically superelastic NiTi). Partial or full overlaying of these tubes will result in a specific shape of the manipulator. Individual tubes are actuated at their base (and are therefore considered extrinsically actuated manipulators) by translating along and rotating about their central axis. Figure 4 shows a three-segment CTM (only the distal part, the actuation mechanism at the base is omitted, but the degrees of freedom per tube are shown).

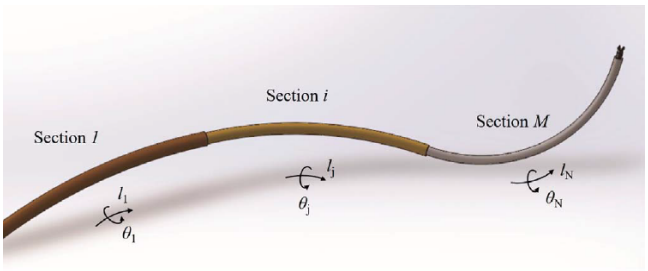

Figure 4: Illustration of structure and components concentric tube manipulator [13].

The pre-curved tube itself is considered to be the transmission mechanism, meaning the CTM design doesn't require any tendon-guiding holes or alternative solutions to force transmission. This leads to a very favourable scalability of concentric tube manipulators. The diameter of CTM is typically in the range of a few hundred micrometers and a few millimeters, making them the preferred design for medical applications like neurosurgery. However the CTM suffers from an issue called *snapping*. This can occur when changing the orientation of a distal tube, due to torsion induced by attempting to rotate the tube fast or uncontrolled. When a tube snaps, it poses serious risks to patient tissue (especially in neurosurgery) as it may leave a cut. When scaling a CTM design up in size, the required torque for rotating a distal tube significantly increases, which is accompanied by an increased risk of snapping. Additionally, torsion can give rise to unstable elastic behaviour [5] making robot shape and behaviour unpredictable.

2.1.4 Recent Advances in Literature

Recent literature shows the focus of flexible manipulator design is laid on the tendon routing. Up to now, the tendon-actuated manipulators were assumed to route the tendons in a simple, linear path of constant radius from and angle to the central backbone. In practice however, this is not always used in tendon-actuated manipulators as for example helical routing is an alternative possibility

that may increase end-effector workspace and dexterity. With helical tendon routing, the tendon-holes of two adjacent spacers that a single tendon passes through are not situated directly above each other in the manipulator's neutral position, but the next tendon-hole along the central backbone is shifted by a constant angle. The resulting deflection when the helically routed tendon is tensioned is no longer a planar arc with constant curvature in the ideal case, but it follows a three-dimensional helical trajectory. The (ideal) trajectory of the manipulator under actuation may not be as intuitively found as with a constant curvature model, but the next subsection will elaborate on modelling techniques of which some can also be applied to non-standard tendon routing patterns.

In 2017, a dedicated paper on the merits of helical tendon routing in continuum robots was published [15]. The paper investigated the effects of helical tendon routing compared to the standard linear pattern. Hybrid (halfway linear, then continuing in a helical pattern) and complex helical (helical tendon that changes winding direction halfway) patterns have been evaluated for the single- and two-segment case with three tendons routed according to the different patterns. Results show that when compared to standard linear tendon routing, helical tendon routing patterns can increase the workspace of a single-segment manipulator by a factor 4, and a two-segment manipulator by a factor 2.5.

Other recent research by Oliver-Butler et al. [16] (2019) shows the effects of a non-parallel or converging tendon routing design. While the pattern may still be considered linear (i.e. adjacent spacers do not change the angle of the tendon in neutral configuration), the tendons are no longer parallel and form a conic shape. Adjacent spacers decrease the distance from the tendon-hole to the spacer centre as you move closer to the end-effector along the central backbone (i.e. adjacent spacers change the tendon radius along the backbone). It is concluded that the converging tendon routing design increases manipulator stiffness. In effect, this means that while the manipulator is less prone to deformation due to external loads, it also requires increased actuation force to move the tip to a reference position.

2.2 Modelling

A robotic flexible manipulator with an accurate model can be precisely controlled for medical applications. Modelling of flexible manipulators is comprised of two main components as described by Burgner-Kahrs et al. [5]: the kinematics and mechanics framework. The former describes the manipulator motion using geometric relations, without considering any external forces into account. In an open environment the end-effector position can be computed from individual joint parameters using a kinematic framework typically referred to as the forward kinematics of a manipulator. The inverse kinematics unsurprisingly describe the relationship that allows for a set of joint configurations corresponding to a known end-effector position to be found. The more complex mechanics framework relates actuation and external loads to manipulator shape

and motion, thus describing the system dynamics. This type of modelling allows for more robust control of the manipulator. In the following subsections some popular and interesting approaches to the modelling of both kinematics and mechanics are presented. It is assumed that the tendons are routed linearly and parallel, unless stated otherwise.

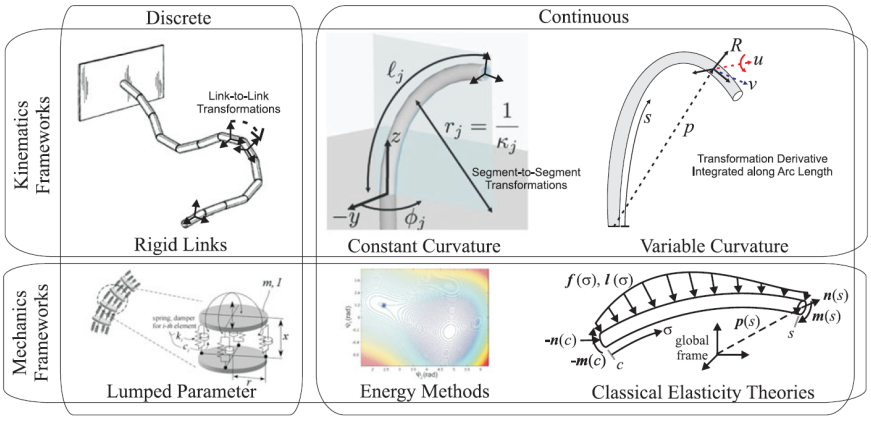

Figure 5: Overview of kinematics and mechanics frameworks frequently used to model flexible manipulators [5].

Figure 5 shows an overview of these approaches, where it becomes clear there are discrete and continuous techniques. Flexible manipulators can be both continuum (TCM, CTM) and discrete (TSM) robots, but are not inherently linked to a corresponding discrete/continuous approach. Continuum robots can be approximated using discrete approaches, and vice versa serpentine manipulators still allow for a continuous approximation when the joint-spacing relative to the total module length is small enough.

2.2.1 Kinematics Modelling

The discrete approach to a kinematics framework uses conventional rigid links (of revolute, universal, or spherical joints) and computes a series of homogeneous transformations. Transformation matrices can be derived using standard approach such as the familiar Denavit-Hartenberg parameters, or using unit twists in screw theory. When the ideal displacement trajectory of the manipulator's tendon routing design is known, the discrete approach can be applied to approximate this trajectory, while this may severely complicate the derivation when a non-linear routing pattern is used.

Continuous geometry may instead be modelled using piecewise constant curvature (PCC). When the actuator's deflection may be approximated with an arc of constant[1] curvature, its kinematics can be modelled in a continuous fashion using some simplifications. PCC models a flexible manipulator by assigning

[1]constant over the arc length, not over time

a set of finite arc parameters to every bending module. The arc parameters describing a module's shape are typically the curvature ($\kappa = \frac{1}{r}$, with r the bending radius of the manipulator), plane (ϕ; which is the angle that the plane in which the manipulator bends makes with a fixed reference plane for which $\phi = 0$), and arc length (l). The latter can however be assumed to be constant in the case that manipulator extension and compression are neglected. A fourth, dependent arc parameter is sometimes also used, which depends on both the curvature and arc length ($\theta = \kappa l$). Therefore, to describe a planar manipulator only two arc parameters from the set $\{\kappa, l, \theta\}$ are required, and an open space (3-dimensional) manipulator is described by two picks from the same set along with the parameter ϕ describing the bending plane. This is conform to the intuition that a planar manipulator is simply an open space manipulator for which the bending plane is fixed.

Variable curvature modelling [17] will typically attempt to fit the manipulator's central backbone to linear combinations of shape functions (e.g. trigonometric functions, clothoids, or wavelets), or a geometrically correct model is formed based on equilibrium conformations of elastic beam theories (such as the Cosserat Rod theory, which will be discussed later as it can serve as a mechanics model as well). While the latter type of variable curvature modelling is a relatively computationally expensive approach for kinematic modelling, the former may be better suited. This modal approach was first proposed by Chirikjian and Burdick [18], and further developed using different shape functions. Independent on the number of discrete subdivisions, this approach will yield a continuous solution. In order to ensure a smooth manipulator shape, an extra condition has to be met, dictating that the first order derivative is a continuous function over the arc length as well.

Recently, in 2014, Mahl et al. [17] translated the PCC approach to a variable curvature modelling method by subdividing every manipulator module into a finite number of smaller subsegments that can be described as CC arcs, each with an independent set of arc parameters. An advantage of this approach over PCC is that it gives a lot of flexibility regarding the trade-off between model complexity and computational cost, as the number of subdivisions could be tuned for every specific application. Whereas the subdivision into only a single 'subsegment' would correspond to the PCC approach, this number may approach infinity in order to approximate a continuum solution (which should in theory be able to be a geometrically exact approach).

Variable curvature approaches may provide the best accuracy for kinematic modelling, and discrete approximations are most accessible for people coming into continuum robotics from the rigid counterpart. The popularity of these kinematic modelling techniques is overshadowed — in recent literature that was investigated in this review — by use of the simple yet effective piecewise constant curvature approach.

2.2.2 Mechanics Modelling

While a kinematic model describes the manipulator's pose in free-space, this resembles a simplified version of reality, where external loads cannot always be neglected. For this cause a mechanics model may be used.

Approximating continuum manipulator mechanics can be achieves by following a discrete approach referred to as lumped parameter mechanics models. Following almost naturally from the discrete kinematics counterpart (rigid link models), this discrete approach can also be imposed on a variable curvature approach. In this type of mechanics model, attaches mechanical elements such as point masses, springs, and dampers to the kinematics framework. The model's governing equations can follow from classical Newton-Euler equations or energy methods.

This latter technique for obtaining the discrete mechanics model of a manipulator can also be used to provide a continuous mechanics model. The review on continuum robots by Burgner-Kahrs et al. [5] reports the following purposes that energy methods have been used for. Control of hyper-redundant robots using elastic energy minimization by applying Euler-Lagrange equations to an elastic energy functional. Similar approaches using energy minimization are also used for constant and variable curvature models of concentric tube manipulators, and analysis of unstable torsional behaviour. The principle of virtual work or power in a lumped-parameter, constant curvature model can lead to intrinsic wrench sensing capabilities or continuum manipulator dynamics. The robot dynamics have also been derived using a Lagrangian approach for both planar and spatial manipulators.

Long, slender objects can be modelled using classical elasticity theories. A widely used constitutive law following from classical Bernoulli-Euler elastica theory — that internal moment is proportional to change in curvature — and its analytical solution in terms of elliptic functions can be used to describe exact mechanics of planar robot curves. Another, very popular, elasticity theory is Cosserat Rod theory. Originally developed by the Cosserat brothers in the 19th century, the theory in general describes the continuum mechanics of any arbitrary deformable surface or by a set of non-linear ordinary differential equations for internal force and moment distributions. Cosserat Rod theory non-surprisingly describes the special case where the shape is a rod, which can lead to some approximations: a special case of Cosserat Rod theory where shear and axial strains along the rod are neglected is described using Kirchhoff Rod theory.

Recently (2019), Chikhaoui et al. [19] have compared two modelling approaches that are Cosserat Rod theory and beam mechanics modelling in a hybrid tendon-actuated concentric tube manipulator with three extensible segments. External loads are applied only at the manipulator's end-effector, and gravity is modelled within a segment as a series of uniformly distributed point loads for the latter model (assumptions made regarding gravitational effects are not explicitly mentioned for the Cosserat Rod model). The classical modelling principle that is the trade-off between model complexity, computational

cost, and model accuracy is seen observed here as well. While the Cosserat Rod model provides more accurate results, the computational effort this takes (mean of approximately 5 frames per second) is substantially higher than for the beam mechanics model (mean of approximately 5000 frames per second). It should however be noted that in another study focussing specifically on Cosserat Rod modelling in both tendon-actuated and concentric tube manipulators [20], the computational cost is reported to be significantly less, as the full control of a 6 DOF concentric tube manipulator was performed at 200-300 frames per second and the model solution along with a Jacobian could be computed at 1000 frames per second (in C++).

The latter study by Rucker [20] extends the standard Cosserat Rod model by adding a coupled tendon model which describes the distributed loads along the manipulator's central backbone that is caused by a tensioned tendon. The paper shows an implementation for the single-segment case only. This coupled rod-tendon model is capable of handling non-standard tendon routing patterns, as is shown for helical and polynomial tendon trajectories. Further expansion of a coupled Cosserat rod-tendon model is presented in 2019 by Oliver-Butler et al. [16], in which the model is adapted to predict deformation of a rod under external loads when the axial displacement of the tendons is kept constant. While in other cases the tendons are assumed to be backdriveable, this model attempts to describe the mechanics of a manipulator with non-backdriveable tendons.

Qi et al. [21] (2018) have investigated the control of a single-segment TCM using a model based on virtual work, where they also paid attention to the non-linear friction that may be present in a tendon-pulley force transmission system. Roesthuis and Misra [22] (2016) have created a rigid-link model with 3D position reconstruction using Fibre-Bragg grating (FBG) sensors (a type of fibre-optic sensor) for controller input to control a TCM consisting of two segments that are assumed to be inextensible. External loads are put on the manipulator's end-effector, and only the planar case is evaluated in the experiments. Additionally, the force sensing capabilities of a manipulator using FBG sensors is investigated, which can also be read about in a follow-up study by the same group [9].

Part I
Design

This part of the thesis focuses on the design of the actuation system. First the requirements for the final prototype system are identified and listed. Then the implementation of the requirements are detailed together with a presentation of the design. Finally, the results of the quantification of the system's performance are given.

3 System Design Requirements

In order to comply to the stated thesis aim, the actuation system has to be designed accordingly. As a first restriction on the design it is noted that a modular approach is taken for a complete endoscopic setup. That is, the actuation system should be designed to function independently from any tendon-based endoscope that is connected, or any deformation compensating/teleoperation control scheme. Further design requirements that should be fulfilled can be extracted from the aim presented in section 1.2. The following paragraphs presents and motivates the requirements that have been identified.

Most obvious is the requirement that a single-segment flexible endoscope has to be actuated by tendons for two-dimensional bending of said segment. More concrete, this poses a restriction on the number of actuators required. In order to bend a tendon-actuated manipulator around two axes of rotation, typically three or four tendons spread around the central backbone are actuated. As will be elaborated on later, using two actuators to actuate two tendons simultaneously is also possible. This means the design should incorporate between two and four actuators to pull on the endoscope's tendons.

Prediction of endoscope deformation can be performed in various ways. To allow the designed system to cover application of most of these approaches, the manipulator's state variables that directly or indirectly describe the entire configuration of the endoscope must be available for prediction. In this thesis, it is assumed that the length of all tendons, the tension in all tendons, and the complete set of external loads acting on the endoscope suffice to derive all possible states the endoscope can be in. The motivation for this assumption is that tendon length and tension (independently or together) can be used to fully control a flexible manipulator in two rotational degrees of freedom, and if external loads on the manipulator are included any disturbances can be modelled as reaction forces and moments if need be. Furthermore, the external loads are assumed to be known at all times in this thesis. Appendix A presents several approaches taken to measure or compute external loads acting on the endoscope, but none of these are implemented at this time. In essence, the requirement on the actuation system design is that it must be able to measure the tendon length and tension, and relay these values to an interface without significant delay to (theoretically) allow real-time deformation prediction using virtually

any approach.

As is stated in the aim, the actuation system should be able to compensate for any predicted deformations. While the logic of predicting the deformation is separated from the actuation system, this does pose a requirement on the latter. Due to the separation of actuation system and prediction algorithm, the two must be interfaced in order to communicate with each other. From the designed actuation system side of things, this introduces the requirement of being able to receive and process control signals related to compensation. These signals are direct control setpoints for the actuators.

Table 1: Overview of design requirements for the actuation system, with the aim it attempts to satisfy listed.

nr	**Requirement**	**Aim**
1	contains sufficient actuators to pull on either three or four tendons	manipulate a single-segment flexible endoscope
2	measure tendon length	enable deformation prediction
3	measure tendon tension	enable deformation prediction
4	relay measured values to the interface	enable real-time deformation prediction
5	capable of receiving and processing updated control signals	compensate external loads with independent computation of control signals

To summarize, the requirements that have been identified are listed in table 1. In addition to the requirements, the intended application is listed as an aim it attempts to satisfy.

4 Implementation

This section presents the approach taken towards implementing the requirements presented in the previous section. Firstly, design choices are discussed regarding their isolated function in section 4.1. Secondly, the complete system is presented. Finally, methods for quantifying the system's performance in regard to the desired aim and design requirements are presented in section 4.3.

4.1 Materials

This subsection describes individual components of the actuation system. Where deemed relevant, design choices are motivated.

4.1.1 Single-Segment Actuation

The endoscope is actuated by changing the relative[2] length of a tendon. Every tendon runs through the base of the endoscope towards an actuation rod or axis, on which it is fixated by means of clamping the tendon with a bolt and nut. When the axis rotates in a specific direction, the attached tendon will be pulled on. This will increase the tension in the tendon and wind it up on the axis, effectively shortening the tendon. Rotating the axis in the opposite direction will unwind and thus lengthen the tendon. The actuation mechanism is illustrated in a 2D cross-section in figure 6. Since the tendon is basically a completely flexible thread, its tension will never take negative values[3]. As a result, effectively lengthening a tendon cannot be achieved through pushing with the tendon as if it were an incompressible thin rod. Instead, tendons are lengthened by unwinding the tendon, and winding (i.e. shortening) an antagonistic tendon (such as a tendon directly opposite from the lengthened tendon, or a combination of two partially opposite tendons).

The behaviour of shortening and lengthening tendons in antagonistic pairs leads to an interesting design and control approach. When two tendons are each others mirrored counterparts (i.e. directly opposite with equal radial distance) and piecewise constant curvature (PCC) is assumed, bending of the endoscope in any plane will result in the sum of the two tendons' lengths to remain constant. This means that the elongation of one of the tendons will always be exactly equal to the shortening of its coupled antagonistic tendon. In practice, this means that two coupled tendons can be attached to the same actuation axis, making sure that one is wound around the axis in a clockwise direction and the other in a counter-clockwise direction to ensure when one tendon winds up the other unwinds by the same amount. When thinking of endoscope scalability when the number of independently controlled segments is increased, this leads to the minimal hardware requirements of only two motors for every segment, while retaining the same endoscope's 3D workspace — still with only two degrees of freedom, however. Since size considerations are not a priority at this stage of the research, all tendons are separately clamped to an actuation axis. Antagonistic coupling of tendons can still be achieved by coupling a tendon pairs in the software.

The tendon axes are stainless steel rods with a diameter of 6 mm and are rotated by mechanically coupling them to DC motors from Maxon. A maximum continuous torque of 0.13 Nm and speed of 1321 revolutions per minute are supported. The motors are driven with 24V, and a DRV8871 DC motor driver breakout board[4] is used in order to control them using a microcontroller's low-voltage PWM outputs. The transmission of the motors is first subjected to a gearbox with a reduction ratio of 5.3:1.

[2] a tendon's relative length is the difference in length of its current configuration compared to the reference length when the endoscope is not bent and all tendons are straight and equal in length

[3] positive tendon tension can be seen as pulling with the tendon, and negative tension as pushing with the tendon

[4] `https://www.kiwi-electronics.nl/adafruit-drv8871-dc-motor-driver-breakout-board`

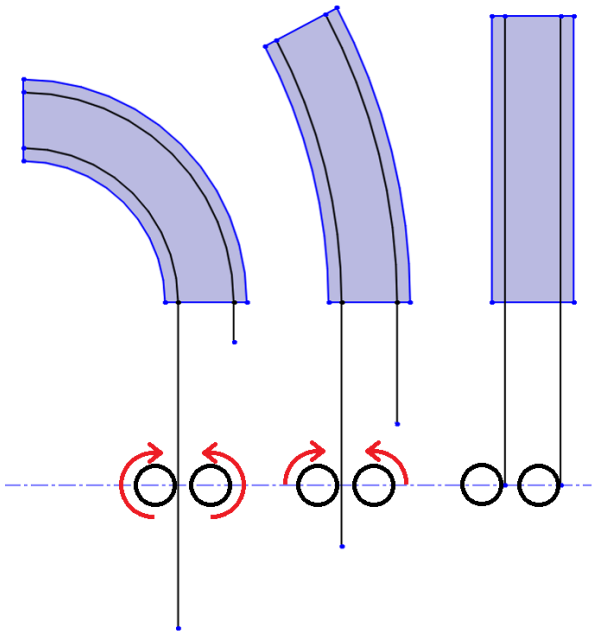

Figure 6: Two-dimensional schematic of the tendon-based actuation mechanism, showing two antagonistic tendons lengthening and shortening (relative to dotted line). Black circles represent axes that un-/wind tendons by a rotation that is denoted with red arrows.

4.1.2 Deformation Prediction

In order to measure tendon length at all times, the motors are outfitted with an optical quadrature encoder that pulses as the motor axle rotates. With 4*1024 pulses per full revolution, a factor 5.3 gear reduction, and knowing that every revolution un-/winds ($2\pi r = 2\pi 3.25 =$) 20.42 mm of tendon, this rates the tendon length resolution at ($20.42/(4 * 1024 * 5.3) =$) 9.4e−4 mm/pulse.

Between a tendon's exit at the endoscope's base and its actuation axis, the tendon is routed along a sensor to measure the tension in the tendon. The tension sensing is achieved by fixing a load cell to the actuation system on one end, and letting the tendon pull on the free end of the load cell. Internally, the load cells contain strain gauges that are very sensitive to strains induced by small deformations of the load cell's aluminium 'shell' that are caused by pushing or pulling on the free end. Multiple internal strain gauges configured in a Wheatstone bridge allow an output voltage to be measured that is proportional to the internal strain caused by a tendon's tension. These analog signals are amplified to a more practical range and converted into digital signals by a HX711 load cell amplifier[5]. The HX711 amplifier board can be sampled at a frequency

[5] `https://www.sparkfun.com/products/13879`

up to 80 Hz.

The tension sensor consists of the load cell previously described, and two core components that are 3D printed using tough PLA, shown in figure 7. One of these parts (right side in the figure) is used to fix the passive end of the load cell to the casing of the actuation system, which is considered to be the static, fixed world. The bolt going through this base can be tightened or loosened in order to increase or decrease the tendon path and thus manually tune the tendon tension. The other end of the load cell (left side in the figure) is fitted with the other 3D printed component, which connects the free end of the load cell to a small axis. Around the axis a thin disc can rotate with a groove to guide the tendon along the tension sensor. The disc contains a ball bearing to reduce the friction between tendon and tension sensor when the tendon is being actuated.

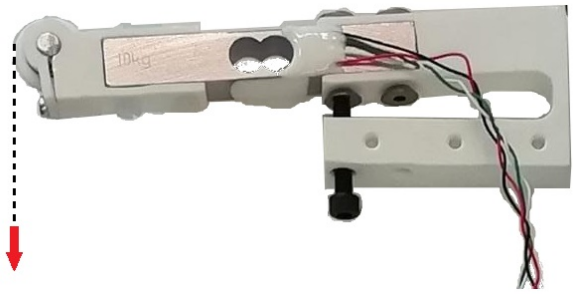

Figure 7: Tension sensing unit. The load cell (in the middle) is encased by 3D printed parts on both sides to fixate it and guide the wire along the sensor. Forces along the dotted line marked with the red arrow are measured.

4.1.3 Interfacing the System

The actuation system's communication to the interface with the 'outside world' is represented by a microcontroller. The microcontroller that has been used is a Teensy3.5, from PJRC[6]. Using interrupt pins, the encoders can immediately update the tendon lengths that are tracked in the microcontroller software. The microcontroller will regularly sample the tension sensors before publishing their measurements to the interface, together with the tracked tendon lengths. The combined sampling-publishing loop can run at 40 Hz, which is expected to be sufficient for real-time control applications.

Control the motors is based on setpoints received from the interface; the values of the setpoints are computed by other software outside of the actuation system. This allows for model predictions and 'outer loop' control signals to be independently computed. Since the microcontroller is programmable it is

[6] `www.pjrc.com/store/teensy35.html`

obviously still possible to implement a control scheme where further processing is performed locally on the Teensy board. In the current implementation, however, the microcontroller will receive four individual setpoints for each of the tendons, expressed in relative tendon length. These setpoints are realized by a low-level control scheme running on the microcontroller at 100 Hz. The control scheme is detailed in section 4.3.2.

4.2 Complete Actuation System

The complete system that combines all previously mentioned components is presented in figure 8. Different sections are labelled to aid in the visualization of the complete setup.

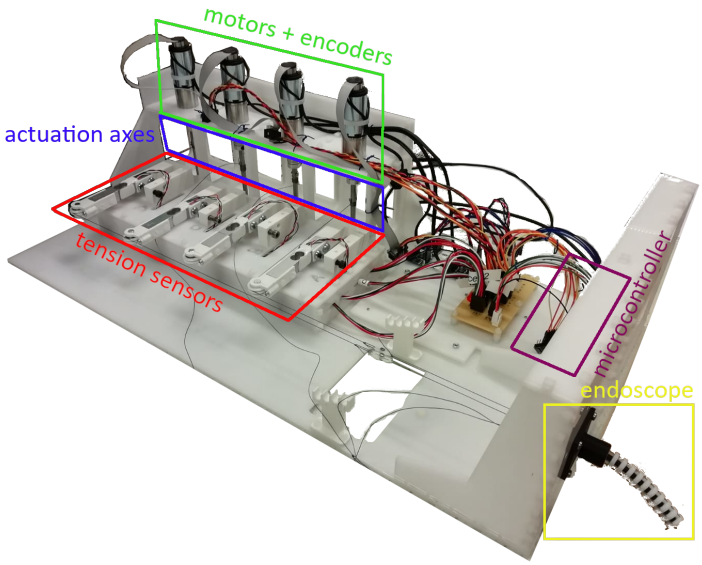

Figure 8: The full actuation system with two connected tendons. Individual components are labelled.

In yellow, a tendon-driven endoscope is shown. The design of this component is disregarded in this subsection, as a modular approach to the design of the actuation system was taken. For more details on the endoscope itself, please refer to section 7.1. At the base of the endoscope (clamped using the black holder), four tendons emerge.

In this specific image, two of these tendons are connected while the other two run loose. The connected tendons run along the tension sensors (in red) where they make a 90 degree bend and are wound on the actuation axes (in blue). The actuation axes are mechanically coupled to DC motors (in green). As mentioned, these motors contain encoders to keep track of the tendon's relative

length. The wiring of the sensors, motor control, and power supply is merged together and then connected to the appropriate pins on the microcontroller (in purple).

4.3 Methods

The following subsections describe the methods that are developed or applied to achieve various tasks. Additionally, experimental approaches are detailed that are used to quantify the system's performance.

4.3.1 Tension Sensing

The tension sensor's hardware has already been described, but the software approach, calibration, and validation protocol are described here. Measurements amplified by the HX711 board are sampled by the microcontroller. Since the microcontroller doesn't require any information regarding the tension in the tendons and it's separated from the 'knowledge center' that does for predicting endoscope deformation, it suffices to sample the raw data and pass it on to the interface.

These measurements are the raw data and cannot be directly interpreted as a force pulling on the tendon. After a calibration of the relationship between the measured raw data values and the true tendon tension force, the values can be processed to represent a force. This is done in the interface, however, to keep the actuation system simple and to keep the processing logic independent from the actuation system.

The measured raw data and the corresponding tendon tension are assumed to have a linear association. Calibration of a tension sensor (load cell + amplifier board) essentially boils down to finding the parameters describing a line or linear relationship that maps the raw data to a value which has a physical interpretation of the tension in the tendon. These parameters are found using a first order (linear) regression algorithm which fits a line through a set of pairs containing a known tendon tension and corresponding measured raw value. The data sets are obtained by hanging a known mass on a tendon that is routed along a tension sensor and sampling a measurement. By allowing the tendon to hang downward (using a ball-bearing to minimize friction) the tension in the tendon is assumed to be known by simply considering the gravitational force acting on the mass. Table 2 summarizes the masses and corresponding tension tendons that have been used for calibration.

Since the use of load cells as tension sensors is intended to meet the requirement to measure tendon tension, an experiment is conducted to evaluate the performance with regards to this specific aim. The performance is assessed by comparing known tendon tensions with measured values. A known tendon tension is applied by hanging a known mass on the tendon running over the tension sensor, just as with the sensor calibration.

Table 2: List of masses and corresponding tendon tensions used to calibrate the tension sensors.

mass [g]	0	5	10	20	30	50	70	100	120	150	200	250
tension [N]	0	0.0491	0.0981	0.196	0.294	0.491	0.687	0.981	1.18	1.47	1.96	2.45

4.3.2 Low-Level Control

In this thesis, antagonistic tendons were not coupled together by hardware, but instead by software restrictions on the motor control. All four tendons are connected to their individual actuation axis, but the setpoints in tendon length that the microcontroller receives are two sets of coupled setpoints. This creates the flexibility of both coupled and uncoupled control by the same microcontroller script.

The setpoints that are received by the microcontroller represent a desired relative tendon length per actuation axis or tendon. Internally on the microcontroller, a separate PID controller is running at a frequency of 100 Hz for every motor. This tendon-length-based PID control loop is referred to as the *low-level control* of the system, as it functions at an individual actuator's level. A higher-level control loop is feasible and would for instance include the manipulator's kinematics or mechanics.

Apart from control on coupled and uncoupled tendon length, the endoscope can also be controlled on a low level by specifying a set of desired tendon tensions to be realized by a simple PID controller using real-time measurements from the tendon sensors. While fairly easy to adapt the code for such purposes, this control approach has not been implemented in this thesis. It should be noted that the only limitation (implementation-wise) is that the calibration logic, including the calibration parameters of the loads cells, is stored outside of the microcontroller. When the load cells are calibrated and not expected to require any additional tuning however, this is easily avoided by moving the processing of raw data upwards and letting the microcontroller handle both reading and processing of sensor data.

In order to evaluate the system's performance specifically in terms of handling control signals that steer the endoscope, a validation experiment is envisioned. In this experiment, the endoscope follows a spatial trajectory by providing the actuation system with a series of updated setpoints (in tendon length). By tracking the endoscope tip's position and the envisioned tip position corresponding to the trajectory over time, an error can be formulated that is used to assess the PID controller's functionality.

5 Actuation System Performance

This subsection presents the results of the performance tests that are described in the previous section. The quantified values should reflect how well the designed system works regarding the design aims that were set. Unfortunately not all experimental data could be gathered due to the lab closing down during the COVID-19 crisis as will be mentioned where there are caveats in the data.

5.1 Tension Sensing

The calibration results of the four tension sensors that have been used in the actuation system are presented in figure 9. The calibrated linear association that is shown maps from mass to raw measurement and should be considered to be the inverse of what is done during the intended processing of raw data.

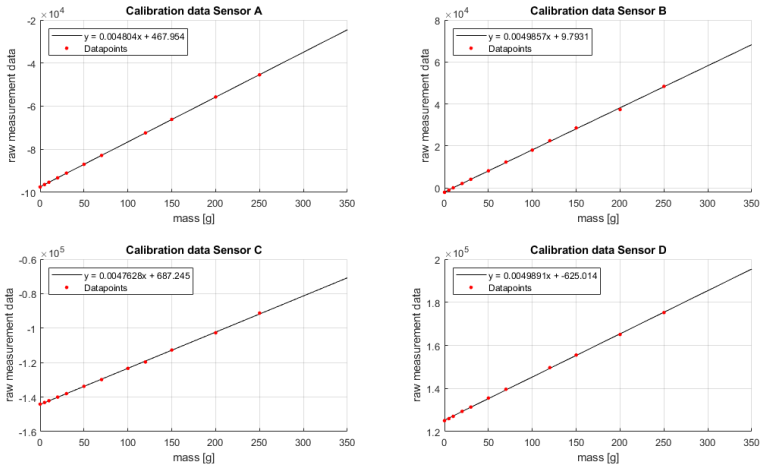

Figure 9: Plot of the calibrated tension sensors. The linear relationship is shown with a line, the discrete calibration pairs are shown with the red data-points. Note that the processing of raw measurements (y in legend) to mass (x in legend) is done using the inverse.

The performance of tension sensors could not be experimentally evaluated due to the lab closing down amidst the COVID-19 crisis, prohibiting access to the setup.

5.2 Low-Level Control

Due to the denied access to the lab, as was mentioned above, this part of the system's validation could not be performed either. This means there are no quantified results on the performance of the low-level controller.

Part II
Model-Based External Load Compensation

In the second part of the thesis, the designed actuation system is evaluated in a practical application where the deformation due to external loads should be compensated for. The first section describes the theoretic basis of the model used to predict the endoscope's deformation. Next, the other materials (hardware- and software-based) are listed and described, and their integration with the designed prototype system from the first part is described. Subsequently, some methods that were used in processing of information or approaches for experiments are detailed in the next section. The results section presents the outcomes of these methods. Finally, the discussion and conclusion are not limited to only the second part of the thesis, but span the general scope including the part on the actuation design, as was mentioned in the introduction.

6 Cosserat Rod Modelling

As mentioned in the literature review, Cosserat Rod theory is a popular approach to modelling an endoscope's mechanics. This section will give a more in-depth description of Cosserat-type models, and specifically the implementation of a coupled Cosserat Rod model for modelling a tendon-actuated endoscope in this thesis.

In the Cosserat theories of continua, a elastic medium has kinematically independent translational and rotational degrees of freedom [23]. Each point of such a deformable medium can be represented as an infinitesimally small rigid body. By relating the stresses and strains that arise due to the translational and rotational degrees of freedom, more complex continuum deformation can be described than using classical elasticity theory where only translational degrees of freedom are considered. The governing equations in general Cosserat continuum theory are found by analysing an object's internal stresses and strains, due to internal and external loads, and are evaluated in a static equilibrium[7], typically under constraints that arise from the medium's surroundings (including external loads, free-space constraints, or physical restraints).

For modelling rod mechanics specifically, Cosserat Rod theory is introduced. Here, a curve describing the rod serves as a deformable structure subjected to the Cosserat elasticity theory. Every point on the curve can be described by a position in space with three deformable vectors, or directors. In some cases one or more of these directors may be rigid in order to comply with no-shear or no-strain assumptions. To simplify relations in the model, in this case the

[7] while in this thesis the Cosserat models are limited to a static evaluation, it is possible to expand them to describe dynamics as well

directors are chosen to be orthonormal vectors resulting in them representing a rotation matrix that the material in the rod's cross-section is subject to.

The prediction of endoscope deformation in this thesis is performed by Cosserat-type modelling. Such a type of model is reported to very accurately predict deformation as a full 6-DOF pose, specifically under out-of-plane loads which can be expected to be present in a clinical application. Furthermore, due to the way the Cosserat model is derived from mechanics theory, it is easily adapted for application to non-standard endoscopes. Think of more complex tendon routing patterns, or pre-formed (non-straight) endoscopes. For these reasons, it is expected that using a Cosserat rod model will provide the most useful predictions for this thesis and further research on the topic. As noted before, however, the high accuracy and wide range of applications of a Cosserat model comes with high computational costs. While not especially relevant for this thesis — as no real-time compensation is attempted, only in the static case — this is a negative note that should be kept in mind. Previous studies by Rucker [20] have designed a custom optimization method — using efficient Jacobian computation — that has provided real-time teleoperated control of a simulated concentric-tube manipulator at $200 - 300$ Hz. Therefore, it is assumed that the high computational requirements do not hamper model-based endoscope control to the point where real-time control is no longer possible.

In the following subsection, the derivation of model equations and their MATLAB implementation are summarized. Please note that the model equations are abstracted from a paper by Rucker [20], with a few minor simplifications applied.

6.1 Model Equations

When the arc that describes the rod as a spatial curve is parametrized by the variable $s \in [0, L]$ which runs from the endoscope's base until its tip (the endoscope has length L in meters), the rod's position anywhere on the arc is given by $\mathbf{p}(s)$, and its rotation matrix by $\mathbf{R}(s)$ (both in a freely defined global frame).

To describe the endoscope's flexible backbone as a Cosserat rod, the following homogeneous transformation can be used to characterize the central curve of the backbone:

$$\mathbf{H}(s) = \begin{bmatrix} \mathbf{R}(s) & \mathbf{p}(s) \\ \mathbf{0}_{1\text{x}3} & 1 \end{bmatrix} \tag{6.1}$$

The linear and angular rates of change of $\mathbf{H}(s)$ w.r.t. s (expressed in the local endoscope's frame $\mathbf{H}(s)$) are given by $\mathbf{v}(s)$ and $\mathbf{u}(s)$, respectively. This leads to the following relationships describing the deformation of the rod:

$$\begin{aligned} \dot{\mathbf{p}}(s) &= \mathbf{R}(s)\mathbf{v}(s), \\ \dot{\mathbf{R}}(s) &= \mathbf{R}(s)\tilde{\mathbf{u}}(s), \end{aligned} \tag{6.2}$$

where the dot operator represents the derivative w.r.t. the arc parameter s, and the tilde operator acts on vectors $\mathbf{x}$ such that $\tilde{\mathbf{x}}\mathbf{y} = \mathbf{x} \times \mathbf{y}$. Reference variables

related to the endoscope's undeformed configuration under the assumption of no external loads are noted with a superscript asterisk. Furthermore, at any position $\mathbf{p}^*(s)$ along the rod, the z-axis of the rotation matrix $\mathbf{R}^*(s)$ is oriented such that it is tangent to the rod's curve. The corresponding x- and y-axes are then always in the cross-sectional plane of the endoscope's backbone and are aligned with the major global axes for simplicity. The exact reference configuration is described in the next subsection where the model implementation is presented. When furthermore the endoscope's reference configuration is a straight rod — like is the case in this thesis — the reference kinematic variables take the following values: $\mathbf{v}^*(s) = \begin{bmatrix}0 & 0 & 1\end{bmatrix}^\intercal$, and $\mathbf{u}^*(s) = \begin{bmatrix}0 & 0 & 0\end{bmatrix}^\intercal$.

The classic forms of the equilibrium differential equations for a Cosserat rod are found by differentiating static equilibrium conditions w.r.t. s. The static equilibrium conditions are obtained in the paper through summing forces and moments applied on infinitesimally small sections of the rod. For a detailed derivation, please refer to the second chapter in the referenced paper. The resulting differential equations describing the equilibrium are:

$$\begin{aligned}\dot{\mathbf{n}}(s) + \mathbf{f}(s) &= \mathbf{0}_{3\text{x}1},\\ \dot{\mathbf{m}}(s) + \dot{\mathbf{p}}(s) \times \mathbf{n}(s) + \mathbf{l}(s) &= \mathbf{0}_{3\text{x}1},\end{aligned} \tag{6.3}$$

with $\mathbf{n}(s)$ and $\mathbf{m}(s)$ the internal force and moment vectors expressed in the global frame, and $\mathbf{f}(s)$ and $\mathbf{l}(s)$ the applied distributed force and moment vectors per unit of s, also expressed in the global frame. Furthermore, we define the backbone's stiffness matrices for shear and extension ($\mathbf{K}_{SE}$) and for bending and torsion ($\mathbf{K}_{BT}$):

$$\mathbf{K}_{SE}(s) = \begin{bmatrix} GA(s) & 0 & 0 \\ 0 & GA(s) & 0 \\ 0 & 0 & EA(s) \end{bmatrix}$$
$$\mathbf{K}_{BT}(s) = \begin{bmatrix} EI_{xx}(s) & 0 & 0 \\ 0 & EI_{yy}(s) & 0 \\ 0 & 0 & E(I_{xx}(s) + I_{yy}(s)) \end{bmatrix}.$$

These matrices characterize the material properties of the backbone; E and G are the Young's and shear moduli, respectively, A is the area of the cross-section, and I_{xx} and I_{yy} are the backbone's second moments of inertia about the principle axes. With these, we can express the relation between the internal force/moment distributions and kinematic variables as follows:

$$\begin{aligned}\mathbf{n}(s) &= \mathbf{R}(s)\mathbf{K}_{SE}(s)(\mathbf{v}(s) - \mathbf{v}^*(s)),\\ \mathbf{m}(s) &= \mathbf{R}(s)\mathbf{K}_{BT}(s)(\mathbf{u}(s) - \mathbf{u}^*(s)).\end{aligned} \tag{6.4}$$

While in fact the relations in equations (6.2) and (6.3) contain all necessary information of the Cosserat rod model, it is simpler to rewrite them in terms of the kinematic variables $\mathbf{v}(s)$ and $\mathbf{u}(s)$ and their derivatives. This is done and presented in the paper by Rucker [20], but not presented in this thesis as the full model is expanded from this intermediate result.

6.1.1 Coupled Tendon Rod Model

The final model couples the previously described Cosserat rod model for the endoscope's backbone with a simple model for its tendons based on a classic Cosserat model for extensible strings. Two assumptions are used for the tendon. Frictionless interaction between the tendon and the channel in the spacer disc it's routed through. Additionally, a tendon's position in the cross-section at a certain point along the backbone is considered to be constant (as if the channel is tightly fit around the tendon).

In order to get the tendon model, the distributed force $\mathbf{f}_{i,d}$ that is applied to every tendon (indexed with subscript i) is derived. First we define $\mathbf{p}_i(s)$ as the tendon path expressed in the global frame (with $\dot{\mathbf{p}}_i(s)$ and $\ddot{\mathbf{p}}_i(s)$ its first two derivates w.r.t. the arc parameter s). The tendon path, or rather the position of the tendon for any length s along the backbone arc, can be found by transforming the tendon's local position in the cross-section — simply given by $\mathbf{r}_i(s) = \big[x_i(s), y_i(s), 0\big]^\intercal$ — to the global frame, using the backbone's pose described by a position $\mathbf{p}_i(s)$ and rotation matrix $\mathbf{R}_i(s)$:

$$\mathbf{p}_i(s) = \mathbf{R}(s)\mathbf{r}_i(s) + \mathbf{p}(s). \tag{6.5}$$

Then, the governing differential equations for an extensible string are derived using the same approach as for the backbone's equations, yielding:

$$\dot{\mathbf{n}}_i(s) + \mathbf{f}_{i,d}(s) = \mathbf{0}_{3\text{x}1}. \tag{6.6}$$

Since the ideal string is completely flexible, internal moments and shear forces are not supported, but only a force representing the tension in the tendon. This tension, expressed in Newton, is noted as τ_i and is always directed along the tangent of the tendon curve $\mathbf{p}_i(s)$. Under the previously mentioned two assumptions, and the knowledge that the string's internal force is tangent, we can derive[8] the following equation for the distributed force applied on a tendon through equation (6.6):

$$\mathbf{f}_{i,d}(s) = \tau_i \frac{(\tilde{\dot{\mathbf{p}}}_i(s))^2}{\|\dot{\mathbf{p}}_i(s)\|^3} \ddot{\mathbf{p}}_i(s), \tag{6.7}$$

To couple the tendon and backbone models, the distributed forces for all n tendons are summed together and presented as a combination of a single set of distributed forces ($\mathbf{f}_{t,d}$) and moments ($\mathbf{l}_{t,d}$) acting on the backbone:

$$\begin{aligned} \mathbf{f}_{t,d}(s) &= -\sum_{i=1}^{n} \mathbf{f}_{i,d}(s) \\ \mathbf{l}_{t,d}(s) &= -\sum_{i=1}^{n} (\mathbf{p}_i(s) - \mathbf{p}(s)) \times \mathbf{f}_i(s) = -\sum_{i=1}^{n} (\mathbf{R}(s)\tilde{\mathbf{r}}_i(s))\mathbf{f}_{i,d}(s) \end{aligned} \tag{6.8}$$

[8] please refer to the previously cited paper by Rucker [20] for a more detailed derivation

These can then be substituted into equation (6.3), explicitly dividing the external distributed loads $\mathbf{f}$ and $\mathbf{l}$ into sums of truly external distributed loads ($\mathbf{f}_{e,d}$ and $\mathbf{l}_{e,d}$), and distributed loads due to tensioned tendons ($\mathbf{f}_{t,d}$ and $\mathbf{l}_{t,d}$). This requires the force and moment distributions given in equation (6.8) to be expressed in terms of kinematic variables $\mathbf{p}$, $\mathbf{R}$, $\mathbf{v}$, and $\mathbf{u}$. To do this, expressions for $\dot{\mathbf{p}}_i$ and $\ddot{\mathbf{p}}_i$ are found by differentiating equation (6.5) twice and substituting the results in equation (6.8).

The paper by Rucker [20] gives a detailed derivation of the explicit model equations, but this derivation is omitted from this thesis since it is not relevant to gaining an understanding of the model's logic or approach, as the derivation consists only of rewriting and substituting the equations that have already been presented and motivated by now. The coupled Cosserat rod model's governing equations can then be written as:

$$\begin{aligned} \dot{\mathbf{p}} &= \mathbf{R}\mathbf{v} \\ \dot{\mathbf{R}} &= \mathbf{R}\tilde{\mathbf{u}} \\ \begin{bmatrix} \dot{\mathbf{v}} \\ \dot{\mathbf{u}} \end{bmatrix} &= \begin{bmatrix} \mathbf{K}_{SE} + \mathbf{A} & \mathbf{G} \\ \mathbf{B} & \mathbf{K}_{BT} + \mathbf{H} \end{bmatrix}^{-1} \begin{bmatrix} \mathbf{d} \\ \mathbf{c} \end{bmatrix}. \end{aligned} \tag{6.9}$$

The following intermediate variables are used to simplify the notation:

$$\begin{aligned} \mathbf{A}_i &= -\tau_i \frac{(\tilde{\dot{\mathbf{p}}}_i^b)^2}{\left\|\dot{\mathbf{p}}_i^b\right\|^3}, & \mathbf{B}_i &= \tilde{\mathbf{r}}_i \mathbf{A}_i, \\ \mathbf{A} &= \sum_{i=1}^{n} \mathbf{A}_i, & \mathbf{B} &= \sum_{i=1}^{n} \mathbf{B}_i, \\ \mathbf{G} &= -\sum_{i=1}^{n} \mathbf{A}_i \tilde{\mathbf{r}}_i, & \mathbf{H} &= -\sum_{i=1}^{n} \mathbf{B}_i \tilde{\mathbf{r}}_i, \\ \mathbf{a}_i &= \mathbf{A}_i(\tilde{\mathbf{u}}\dot{\mathbf{p}}_i^b + \tilde{\mathbf{u}}\dot{\mathbf{r}}_i + \ddot{\mathbf{r}}_i), & \mathbf{b}_i &= \tilde{\mathbf{r}}_i \mathbf{a}_i, \\ \mathbf{a} &= \sum_{i=1}^{n} \mathbf{a}_i, & \mathbf{b} &= \sum_{i=1}^{n} \mathbf{b}_i, \end{aligned} \tag{6.10}$$

$$\begin{aligned} \mathbf{c} &= \mathbf{K}_{BT}\dot{\mathbf{u}}^* - \tilde{\mathbf{u}}\mathbf{K}_{BT}(\mathbf{u} - \mathbf{u}^*) - \tilde{\mathbf{v}}\mathbf{K}_{SE}(\mathbf{v} - \mathbf{v}^*) - \mathbf{R}^\intercal \mathbf{l}_{e,d} - \mathbf{b}, \\ \mathbf{d} &= \mathbf{K}_{SE}\dot{\mathbf{v}}^* - \tilde{\mathbf{u}}\mathbf{K}_{SE}(\mathbf{v} - \mathbf{v}^*) - \mathbf{R}^\intercal \mathbf{f}_{e,d} - \mathbf{a}, \end{aligned} \tag{6.11}$$

with $\dot{\mathbf{p}}_i^b$ the first spatial derivative (w.r.t. s) of the tendon path expressed in the local body-frame, given by:

$$\dot{\mathbf{p}}_i^b(s) = \tilde{\mathbf{u}}(s)\mathbf{r}_i(s) + \dot{\mathbf{r}}_i(s) + \mathbf{v}(s). \tag{6.12}$$

This describes the complete endoscope and its deformed state under external loading. The distributed external loads are already incorporated in equation (6.11), but the external point forces $\mathbf{f}_{e,p}$ and moments $\mathbf{l}_{e,p}$ have to be incorporated in the boundary conditions. Additionally, the termination of each tendon

applies a point force $\mathbf{f}_{t,p}$ and moment $\mathbf{l}_{t,p}$ at the point of termination (at $s = L_i$) which is also integrated in the boundary conditions. The tendon termination loads, expressed in the local body-frame (denoted with superscript b), are found as follows:

$$\begin{aligned}\mathbf{f}^b_{t,p}(L_i) &= -\tau_i \frac{\dot{\mathbf{p}}^b_i(L_i)}{\left\|\dot{\mathbf{p}}^b_i(L_i)\right\|},\\ \mathbf{l}^b_{t,p}(L_i) &= -\tau_i((\mathbf{R}(L_i)\mathbf{r}_i(L_i)) \times \frac{\dot{\mathbf{p}}^b_i(L_i)}{\left\|\dot{\mathbf{p}}^b_i(L_i)\right\|}).\end{aligned} \tag{6.13}$$

6.1.2 Boundary Conditions

In order to solve the model equations given in equation (6.9), initial conditions for the kinematic variables need to be given. The endoscope's base (where $s = 0$) has a position and orientation in the global frame which are used for $\mathbf{p}(0)$ and $\mathbf{R}(0)$. The initial conditions for $\mathbf{v}$ and $\mathbf{u}$, when there is no external loading, are trivial as the rod is not deformed and thus takes its reference configuration for which $\mathbf{v}^*(s)$ and $\mathbf{u}^*(s)$ are already known at $s = 0$. When there is external loading, however, these are not necessarily known at $s = 0$, but can appear anywhere along the rod where a point load is applied. In order to solve the model numerically, the initial values at $s = 0$ must be deduced from specified boundary conditions at other positions where $s \neq 0$.

If at a location $s = \sigma$ along the backbone point loads $\mathbf{F}(\sigma)$ and $\mathbf{L}(\sigma)$ appear — due to tendon termination and/or external disturbances — they change the internal force/moment distributions across the boundary at $s = \sigma$ as follows:

$$\begin{aligned}\mathbf{n}(\sigma^-) &= \mathbf{n}(\sigma^+) + \mathbf{F}(\sigma),\\ \mathbf{m}(\sigma^-) &= \mathbf{m}(\sigma^+) + \mathbf{L}(\sigma),\end{aligned} \tag{6.14}$$

where locations σ^- and σ^+ are just before and after $s = \sigma$ where the load is applied. These relations can be rewritten in terms of kinematic variables using the given definitions for the internal force/moment distributions in equation (6.4). The specific implementation of the boundary conditions is described in the following subsection.

6.2 Implementation

The coupled Cosserat model that has been described above is implemented in MATLAB R2019b. The model equations in (6.9) are numerically solved using the standard `ode45` function, which uses a six-stage, fifth order Runge-Kutta scheme with adaptive step-size. Since the specified problem is a boundary value problem, it is solved using a shooting method based on the non-linear optimization (using standard function `fsolve` and its default trust-region dogleg algorithm) of initial values such that it minimizes a residual function that has been defined.

The residual function returns an error vector $\boldsymbol{\varepsilon}$ for the estimated initial values for $\hat{\mathbf{v}}(0)$ and $\hat{\mathbf{u}}(0)$ that are used. The external loads (apart from gravity) in this thesis are only applied as point forces at the endoscope's tip ($s = L$, with L the length of the endoscope in meters), and therefore coincide with the tendon termination loads, further simplifying the integration of boundary conditions. The error is computed by comparing the estimated value of $\hat{\mathbf{v}}(L)$ and $\hat{\mathbf{u}}(L)$ with the expected values ($\mathbf{v}_{ref}(L)$ and $\mathbf{u}_{ref}(L)$) which include the external forces and tendon termination loads for the currently estimates endoscope configuration. The optimization is then handled by the standard MATLAB algorithms, and a set of initial values $\mathbf{v}(0)$ and $\mathbf{u}(0)$ are found that give an endoscope configuration that best matches the specified boundary conditions. The error vector $\boldsymbol{\varepsilon}$ is thus computed as follows:

$$\begin{aligned} \boldsymbol{\varepsilon} &= \begin{bmatrix} \hat{\mathbf{v}}(L) \\ \hat{\mathbf{u}}(L) \end{bmatrix} - \begin{bmatrix} \mathbf{v}_{ref}(L) \\ \mathbf{u}_{ref}(L) \end{bmatrix} \\ \mathbf{v}_{ref}(L) &= \mathbf{v}^* + \mathbf{K}_{SE}^{-1}(\mathbf{R}(L)^\intercal \cdot \mathbf{f}_{e,p} + \mathbf{f}_{t,p}^b) \\ \mathbf{u}_{ref}(L) &= \mathbf{u}^* + \mathbf{K}_{BT}^{-1}(\mathbf{R}(L)^\intercal \cdot \mathbf{l}_{e,p} + \mathbf{f}_{t,p}^b). \end{aligned} \tag{6.15}$$

The locally expressed point loads due to tendon termination are computed by summing the individual termination loads, computed as presented in equation (6.13).

With these given equations, a tendon-actuated endoscope's deformation can be fully predicted. In order to model the gravitational pull on the endoscope, its effects are modelled as a distributed force $\mathbf{f}_{g,d}$ all along the endoscope's backbone. The gravitational acceleration vector is given by $\mathbf{g} = \begin{bmatrix} 0 & 0 & -9.813 \end{bmatrix}^\intercal$ and is expressed in the global frame. This means the distributed gravitational force can be computed as follows:

$$\mathbf{f}_{g,d}(s) = \rho(s) \cdot A(s) \cdot \mathbf{g}, \tag{6.16}$$

with ρ the density in $[kg/m^3]$. Under the assumption that the endoscope's density and cross-sectional area $A(s)$ are constant over s, the gravitational force can also be approximated without requiring to know the exact density of the material by the following:

$$\mathbf{f}_{g,d}(s) = \frac{m}{L} \cdot \mathbf{g}, \tag{6.17}$$

where m is the mass of the entire endoscope in $[kg]$. The effect of gravity on the backbone is implemented this way, but the gravitational effects on the tendons is neglected due to their small mass. The tendon's mass is however included in the mass of the complete endoscope in the above equation.

The model equations are now fully defined, and can be numerically evaluated if the initial position and orientation are known. Since all variables related to position are expressed relative from the endoscope's base, which cannot deform, the initial position $\mathbf{p}(0)$ can be chosen arbitrarily. Similarly, the initial orientation $\mathbf{R}(0)$ can be chosen to fit any desired orientation. For simplicity's sake, the initial position is chosen to be at the global frame's origin. The initial orientation should only correspond to the previously chosen convention that

the local z-axis should be directed along the endoscope's backbone. Since the global frame's gravity vector is directed along the negative z-axis, this means the identity rotation corresponds to a configuration where a straight endoscope is pointing right upwards. Reference configurations where the straight endoscope points along the x- or y-axis requires the initial orientation to be a rotation matrix corresponding to 90 degrees rotation about the y- or x-axis, respectively. Any other initial configurations can also be accommodated for this way.

Finally, it should be pointed out that model evaluation can be fairly complex or simple based on a chosen endoscope design and approximations. The assumptions adopted during this thesis are mentioned in this paragraph. Firstly, the backbone's stiffness matrices $\mathbf{K}_{SE}$ and $\mathbf{K}_{BT}$ are assumed constant along s. Secondly, by endoscope design, the tendon's local position in the cross-section $\mathbf{r}_i$ is assumed to be constant for every tendon as well, with a radius and angular offset from the cross-section center. This leads to the tendon path in the global frame (see equation (6.5)) to be an arc with constant offset from the central backbone arc, while still accounting for torsional bending however, as well as its derivatives w.r.t. s ($\dot{\mathbf{r}}_i$ and $\ddot{\mathbf{r}}_i$) to be zero. Finally, as was already mentioned before, the endoscope's density and cross-sectional area are assumed to be constant along s in the approximation of gravitational forces.

7 Materials

This section describes the materials (hardware and software) that are used to control a tendon-driven endoscope. The actuation system is omitted from this section as it has already been described previously, in section 4.2. Figure 10 shows an endoscope that is actuated in 2D (planar movement using two tendons) by changing control signals on a laptop that is connected to the system. The separate components that the system is comprised of are discussed in the following subsections.

7.1 Tendon-Actuated Continuous Manipulator

In order to carry out validation experiments on external load compensation, a flexible endoscope has been designed. The endoscope design is in accordance with a TCM, containing a single flexible backbone and rigid discs spread evenly along the backbone with evenly distributed tendon routing holes. A single endoscopic segment is actuated using a set of four tendons.

The endoscope segment is manufactured using 3D printing technology. The Objet260 Connex3 is a high resolution printer that can be used to print both rigid and flexible structures in a single design. This is very convenient for the precise manufacturing of a TCM structure which contains both rigid and flexible parts (the spacer discs and backbone, respectively). For this reason, the aforementioned 3D printer stationed at the RAM prototyping lab in the University of Twente has been used to print the endoscope in one piece, using the materials VeroWhite for the rigid components and a mixture of VeroWhite

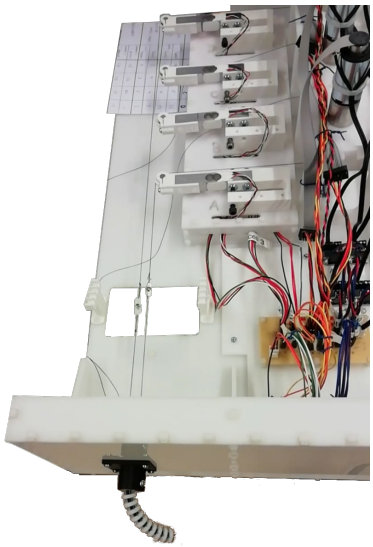

Figure 10: Picture of the actuation system while it is controlled for an endoscope moving in a plane.

and (primarily) AgilusBlack (material mixture code: FLX9870-DM) for the flexible components.

The TCM has been designed in SOLIDWORKS (2018). During this thesis, a single segment has been used, which can be seen in figure 11. The isometric view of the entire endoscope (figure 11a) shows three balloon-like protrusions at the tip, which can be used to connect independently used components such as EM probes, as will be described later. At the endoscope's base, two radial protrusions are seen which are used for locking the endoscope's orientation when it is clamped in the actuation setup. A cross-sectional view of a partial endoscope-segment is shown in figure 11b. Apart from some dimensions, the shape of the tendon routing holes can be seen. Furthermore, it becomes apparent that the flexible backbone is fitted with an inner rigid insert. This rigid insert has a diameter of only $1mm$ in order to greatly increase the backbone's compressional stiffness, while retaining a relatively low bending stiffness. Finally, the spacer discs contain chamfers around their inner perimeter. This reduces the contact surface between the rigid spacers and flexible backbone and is intended to improve the durability of the endoscope when it is required to bend at increasingly big angles. The endoscope has a length of 60 mm (excluding the connector-protrusions), outer diameter of 12 mm (neglecting the orientation locks at the base), and contains 10 spacers if the base — which is clamped in a practical setup — is not counted.

A top view schematic of the spacer discs (including backbone and the rigid insert) are seen in figure 12. As is shown here, there are eight tendons that can

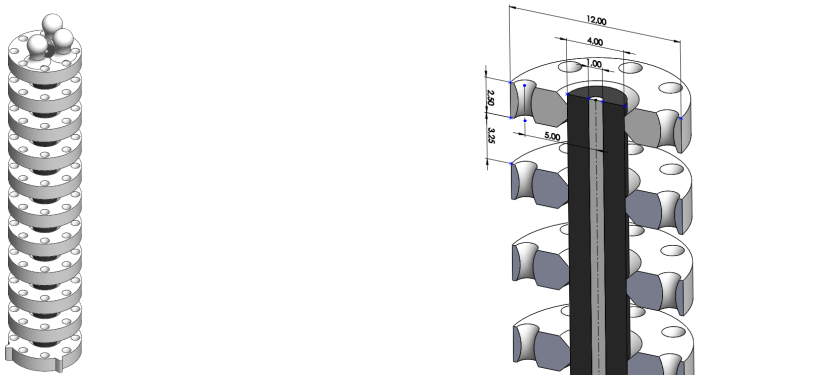

(a) (b)

Figure 11: Snapshots of the tendon-driven continuum manipulator designed in SOLIDWORKS consisting of rigid (white) and flexible (black) parts. Dimensions are in millimeters.

be routed along the endoscope that was used. Since the endoscope is treated as a single-segment endoscope in this thesis, only four (90 degrees spaced) tendon holes are used. These tendons are terminated with a knot right after passing through the spacer disc at the tip. The same endoscope can be extended to a multi-segment endoscope simply by adding another set of four tendons, routing them through the four empty routing holes, and terminating them after a disc somewhere halfway along the endoscope backbone. In theory, the design allows for easy extension to even more independently actuated segments while still being printed as a single structure. The dimensions of the currently used design (especially the diameter of the spacers is a bottleneck) should in theory be capable of routing up to 16 tendons (corresponding to four segments) without requiring a more complex tendon routing configuration.

The spacers dimensions are kept constant all along the endoscope's backbone. This means the tendons' radial distance from the center and angle in the cross-section are kept constant, hence giving a simple linear tendon routing pattern. Different routing patterns have not been explored in this thesis.

The tendons that were used are braided fishing line from *Spiderwire* with a thin coating to limit fraying. These wires are very strong (up to 49.2 kg tension) and have a small diameter (0.40 mm). Since they are non-elastic, their extension when tensioned is assumed to be negligible.

When the endoscope is clamped to an outer wall of the actuation system to be used, the tendons running through the endoscope's spacers should be attached to the tendon in the actuation system that is fixed to the actuation axis. The pairs of tendons are rigidly connected by lasercut connectors that are knotted to the joining ends of the tendons. These connectors allow an M1.4

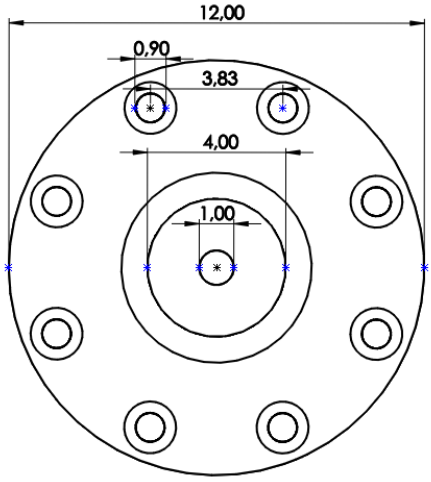

Figure 12: Top view of spacer disc, with dimensions in millimeters.

bolt to pass through and be tightened with a nut to rigidly join the connectors together.

After the tendons have been connected, they are still hanging loose and shortening a tendon will therefore not actuate the endoscope unless the tendon is tensioned. This is achieved by simply winding a tendon up its actuation axis until it is pulling on the endoscope and thus bending it. To allow a consistent reference position of the endoscope to be achieved, bending of the endoscope is restricted when the tendons are being tensioned. The restricted motion of the endoscope is achieved by encapsulating it with a tightly fit '*reference holder*' which is 3D printed by the Objet260 Connex3 using the rigid material VeroClear (a transparent version of the previously mentioned VeroWhite). This allows the tendons to be individually tensioned without disrupting the other tendon's tension by bending the endoscope.

7.1.1 EM Tracker Integration

In order to track the endoscope during any validation experiments, a moulded cap for the endoscope's tip is attached. The cap contains two puncture holes that can each house a needle-shaped EM probe and provide a 5-DOF pose (full position, and orientation excluding rotation around the axis represented by the needle/probe itself). The EM probes that are used are manufactured by NDI Medical (part number 610090) and have dimensions of 0.8 mm in diameter and 11 mm in length.

The two probes are both in a plane parallel to the endoscope's front face, but their projections on the cross-sectional plane of the endoscope are perpendicular. This allows the rotational axis to which each probe is blind to be compensated

for by the other probe.

The connector is moulded using EcoFlex 0050 (a silicone rubber). While in fact a flexible material, it is assumed stiff enough for a rigid approximation in this setup because of its small dimensions and little interference from outside. With only the very thin wiring from the EM probes, gravity, and manipulator motion as possible causes for internal deformation, the positions of the two EM probes relative to each other and the endoscope are considered to be constant.

Figure 13: Close-up on the endoscope with the 6-DOF EM tracker connected. The two wires running out the cap on the endoscope are from the two 5-DOF EM probes.

7.2 Interface

For communication with the actuation system, an interface runs on a connected laptop. The interface is made in ROS, which is robotics middleware. It is a set of software libraries and tools, and allows easy reusability of code through abstraction into 'software containers' that have a distinct function, referred to as packages. ROS provides a framework for fast and easy communication between packages, which makes it a suitable choice for the modular design approach that is followed here.

The actuation system has two outgoing message streams, containing the tension sensor's raw data, and the tendon's measured lengths. The latter is currently unused, but is included in order to have access to all the endoscope's state variables (as was mentioned in the first part). The raw tension sensor data is processed by a dedicated node that contains the calibration data and could recalibrate if need be. It could be argued this node is part of the actuation system's package, but to stick with the modularity, it is classed as a general interface component.

It is envisioned that in a working setup, a predictor package in ROS can receive the measured tension in the tendons, and compute predictions. Working together with a model-based controller that can implement compensation based on predictions, the control signals are computed. These values are passed on to the actuation system through the interface, for them to be realized by the local low-level PID controller.

In reality, the model evaluation is performed in MATLAB after some efforts of coding the model in a C++node in ROS have shown to be a dead-end for this thesis. The complete ROS architecture containing all software implementations can be found online in a git repository from the Robotics and Mechatronics research group [9].

8 Methods

8.1 EM Tracker Integration

Reading out a 6-DOF pose at the endoscope's tip is done by fusing two 5-DOF trackers together. The EM probes are sampled (at 40 Hz) by third party software (OpenIGTLink based) running on a separate desktop pc. A server is also running on the same software that serves as a bridge between the OpenIGTLink software and ROS, publishing all sampled poses on the ROS network that the interface is connected to.

The 5-DOF measurements can be received and processed in MATLAB, where they are fused together. As the positions of the two probes relative to the endoscope tip is assumed to be constant, the fused position is simply taken to be the tracker closest to the tip. Positions are expressed relative to an absolute initial position which is sampled when the endoscope is in it's reference configuration.

The two-dimensional orientation for every EM tracker is initially expressed in quaternions (with the fourth element equal to 0). After translation to a rotation matrix using MATLAB's function `quat2rotm`, the rotation is encoded into a set of three axes describing the new frame. Of these three axes, only one is relevant, as the other two are in a plane perpendicular to the one axis. Any rotation within this plane, or around the 'major' axis corresponds to the 6th dimension in the pose which the 5-DOF EM trackers cannot obtain. Therefore the orientation of the 5-DOF trackers is expressed as a normalized 3D vector; which is seen as the z-axis in the rotation matrix, or the values in the third column. If for one of the 5-DOF trackers (subscript i to distinguish between the two 5-DOF trackers) a set of quaternions $\mathbf{q}_i$ is measured, the corresponding rotation vector $\mathbf{r}_i$ is found as shown here:

$$\mathbf{r}_i = f(\mathbf{q}_i) \cdot \begin{bmatrix} 0 & 0 & 1 \end{bmatrix}^\intercal, \tag{8.1}$$

where $f(\mathbf{q})$ is the MATLAB function `quat2rotm` that translates a set of quaternions $\mathbf{q}$ to a rotation matrix $\mathbf{R} = \begin{bmatrix} \mathbf{r}_x & \mathbf{r}_y & \mathbf{r}_z \end{bmatrix}$.

Since, by hardware design, the two EM trackers are perpendicular to each other, their measured orientations expressed as 3D vectors can be interpreted as two axes of an orthonormal frame. This frame will represent the orientation of the endoscope at the tip, and with its position the full 6-DOF pose is described. The rotation matrix that maps from global coordinates to the local frame at

[9] `https://git.ram.eemcs.utwente.nl/impact/tendon_driven_endoscope/tendon_endoscope_cr_control.git`

the endoscope tip will then contain the x-, y-, and z-axes in each row. The first two are simply the measured 3D orientation vectors for both EM trackers, and the latter is computed by taking the cross product between the x- and y-axes (as this produces a normalized vector that is perpendicular to both):

$$\mathbf{R}_{tip} = \begin{bmatrix} \mathbf{r}_1 & \mathbf{r}_2 & (\mathbf{r}_1 \times \mathbf{r}_2) \end{bmatrix}. \tag{8.2}$$

8.2 Stiffness Characterization

Since the coupled Cosserat model requires the endoscope backbone's stiffness matrix to be known, the Young's and Shear moduli need to be obtained. While these values are a material's properties and could therefore be obtained through any supplied information from the 3D printer's materials, this is not how it is done in this case. The backbone contains both flexible and rigid sections, but it is modelled as a single solid piece with constant stiffness. Therefore, a Young's and Shear modulus for the combined materials have to be obtained instead. This subsection details the approach taken to deduce these values.

Through the comparison of a measured tip position and a predicted tip position using set stiffness values, actual moduli can be deduced. The set of stiffness values is manually tuned to optimize for the magnitude of the 3D positional error between measured and predicted endoscope tip positions. A more detailed experimental protocol is described below.

The endoscope is actuated by applying loads on the endoscope tip (directed straight down using gravity). The end-effector's position in 3D space is tracked using the EM tracker. To limit the number of deformation sources, the endoscope's tendons are uncoupled in this experimental setup. This means the endoscope is only subject to a gravitational distributed force, and a downwards directed point force at the tip. The force at the tip takes one of three values, 0, 0.0491 and 0.0981 Newtons (masses of 0, 5 and 10 grams, respectively).

While conducting the experiment, the masses are applied to the endoscope and it is given some time to stabilize its position (i.e. the swinging mass should not show any movement). When stable, the position is saved, and the next load is applied. This continues until all three loads are cycled through twice, yielding six datapoints.

For every datapoint, the model is evaluated multiple times, each using a different set of Young's and Shear moduli to cover a relatively wide range of stiffness values. The boundaries of the range are initially randomly estimated, but then adapted to include the specific values we're interested in.

These optimal values are found by looking for a local minimum in the total prediction error — which is defined to be the sum of the absolute errors for every prediction (so the magnitudes of prediction error for all six datapoints summed together). Around the local minimum, the predictions are performed again, using a grid of Young's and Shear moduli that are spaced closer together, in order to improve the resolution of the parameter optimization. The resolution that is aimed for is approximately 1%.

8.3 Experimental Model Validation

The experimental validation of the coupled Cosserat model is described in this subsection. In order to answer the third supporting research question, the precision of predictions made with the model is evaluated. This should quantify how well endoscope deformation due to a given set of external loads is predicted and thus validate the model's predictive performance.

In the experiment, the endoscope takes multiple different configurations for which the deformation is predicted. The configurations use varying endoscope orientations and external loads at the tip of the endoscope. Attached to the tip of the endoscope is the moulded EM tracker that — after some post-processing — gives a 6-DOF reference pose which is considered to be the ground truth. It is assumed that the direction and magnitude of all external loads are known, including the effects of gravity which are approximated using the measured weight of the endoscope. Using these known loads and the tension in the tendons which is measured, a prediction of the endoscope's pose is made using the model.

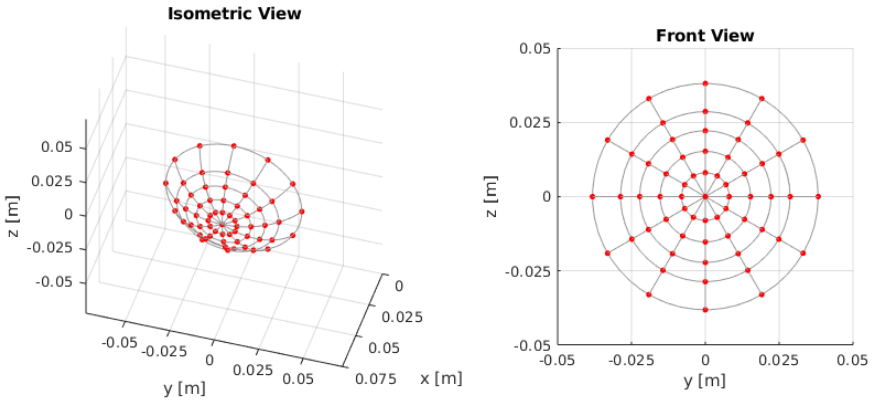

Figure 14: Isometric and front views of the different reference configurations that are used. The configurations are essentially points on the shell of a sphere. Connecting lines are used to visualize what configurations use the same curvature or bending plane (angle ϕ in PCC terms).

Figure 14 shows the different (idealized) configurations that are evaluated. The range of configurations takes the form of a fairly equal distribution of endoscope tip positions across its workspace. The positions of the tip are samples from all possible combinations of a set of curvature values (κ) and plane angles (ϕ) under the PCC assumption, mentioned in section 2.2.1. The actuation parameters for the endoscope to reach every configuration are defined by a set of tendon lengths that correspond to the given configuration under the PCC assumption. It should be noted that in practice, the PCC assumption does not hold. Therefore these computed reference configurations are only estimates that are used to check that the different configurations are distributed well over the

workspace of interest. The configurations, including loaded variants, are defined by the following sets of the three parameters curvature (κ) in 1/m, plane (ϕ) in degrees, and mass (m) in grams:

$$\kappa \in \begin{Bmatrix} 0 & 4.5 & 8.7 & 13 & 17.5 & 26.2 \end{Bmatrix}$$
$$\phi \in \begin{Bmatrix} 0 & 30 & 60 & 90 & 120 & 150 & \dots & \\ & \dots & 180 & 210 & 240 & 270 & 300 & 330 \end{Bmatrix}$$
$$m \in \begin{Bmatrix} 0 & 5 & 10 \end{Bmatrix}$$

While the model computes a position and orientation (i.e. a 6-DOF pose) of discrete points all along the endoscope backbone, only the pose at the tip is used for model evaluation since the EM trackers only provide a reference pose at this point. If any fundamentally wrong predictions of the complete backbone's pose are visually observed, however, these will be reported in the results/discussion section. The 'true' measured and predicted poses are evaluated based on correspondence. In order to obtain an objective measure of the model's performance, a quantity is computed for every configuration. This quantity is the positional error e_p.

A predicted variable x uses the notation: $\hat{x}$, and a variable x considered to be the ground truth is denoted by a superscript star $x^\star$ (not to be confused with an asterisk, referring to a reference configuration such as $\mathbf{v}^*(\mathrm{s})$ and $\mathbf{u}^*(\mathrm{s})$). The positional error is the absolute distance between the predicted and measured positions of the endoscope tip expressed in millimetres:

$$e_p = \|\hat{\mathbf{p}} - \mathbf{p}^\star\| \tag{8.3}$$

When conducting the experiments, the endoscope is initially fixed in its reference configuration using the 3D printed holder that has been described earlier. While the endoscope is fixed, it is tensioned by winding all tendons manually until a desired tension between 1.2-1.5 N is achieved. Then the holder is released, and the endoscope is free to move to a desired 'unloaded' configuration (only gravitational loading). Subsequently, external loads are applied at the tip of magnitudes 0.0491 and 0.0981 Newtons (masses of 5 and 10 grams, respectively) facing downward. Meanwhile, the endoscope's tendon lengths are kept constant.

The endoscope tip's pose is measured using the 6-DOF EM tracker system, and the applied tendon tensions are measured. This set of 'system variables' is measured for every initial configuration in its unloaded, partially loaded (0.0491 N), and fully loaded (0.0981 N) state. Deformation predictions are computed using the coupled Cosserat model and compared to the 'true' (EM-based) deformation.

When predictions made by the model significantly differ from reality, additional predictions are shown in the results. These extra predictions are done using altered parameters of the whole endoscopic system, which may provide some extra insight on the source of the observed errors. Parameters that may be changed can include the measured tendon tension, the weight of the endoscope, and the magnitude of the external force at the tip. The choice of altered

parameters is based on the evaluation of the initial data, and will therefore be motivated in the discussion.

9 Results

This section presents the results of the methods previously described. When relevant, any observations are pointed out. The interpretation of results will not be handled until the next section.

9.1 Stiffness Characterization

Figure 15 presents the results of the optimization of the stiffness parameters. The optimal Young's and Shear moduli are:

$$E = 8.2414 \cdot 10^6 [\text{Pa}], \qquad G = 4.7586 \cdot 10^4 [\text{Pa}].$$

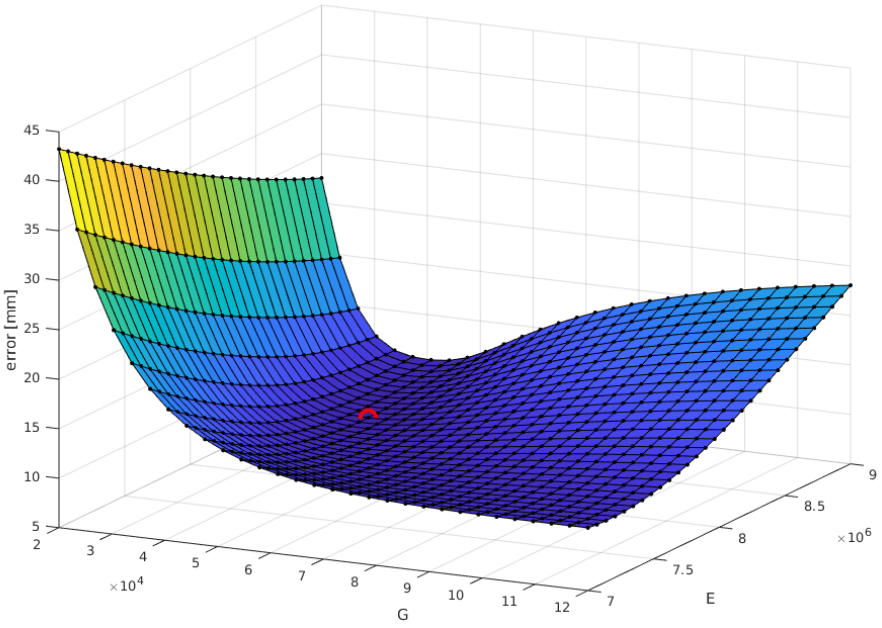

Figure 15: MATLAB figure plotting the cumulative prediction error versus stiffness parameters Young's modulus (E) and Shear modulus (G), both expressed in Pascal. The datapoint for the optimal values is circled in red

The individual errors (as well as the cumulative error) for all used measurement that was performed for the stiffness characterization is shown in figure

16. As can be seen here, the duplicate measurement for the unloaded (0 gram) situation is not included. Since this measurement showed very little cohesion with the other measurements — for which the optimal stiffness values could be found within the same range as is seen in the figure — it is treated as an outlier and was disregarded in computation of the cumulative error.

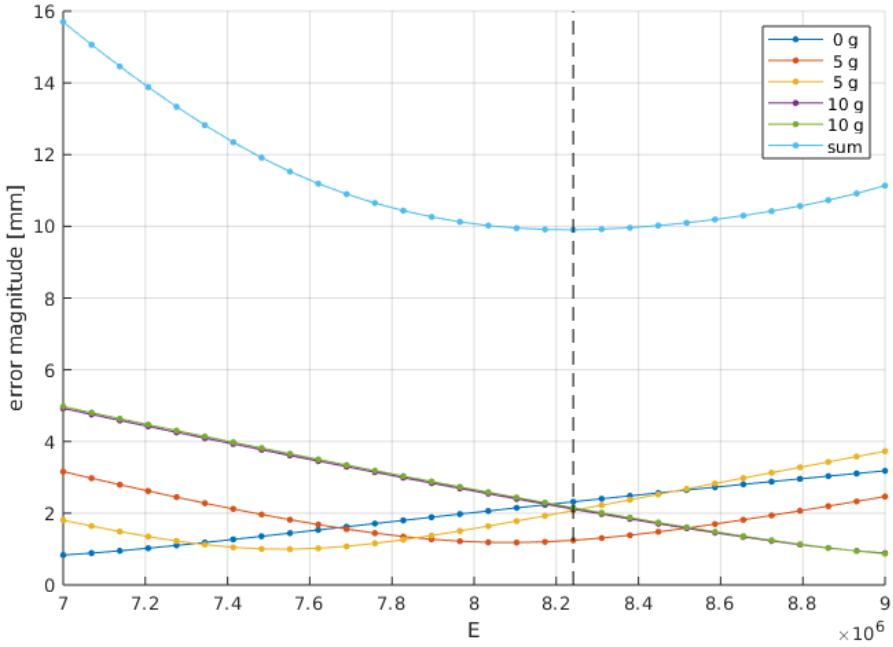

Figure 16: MATLAB figure plotting the cumulative and individual prediction errors versus stiffness parameter Young's modulus (E) for the previously found optimal Shear modulus (G). The dashed vertical line corresponds to the optimal Young's modulus.

9.2 Experimental Model Validation

The following figure 17 presents the positional prediction error that is computed according to equation 8.3. The magnitude of the error is expressed in millimeters. The data is split per external load applied and per intended radius of curvature. Missing datapoints correspond to configurations for which the model could not find a valid solution and are therefore left out.

The plots in figures 18 to 20 show the individual errors in the (global) x-, y-, and z-coordinates. What can be observed here is that the error in the z-coordinate only takes positive values independent on what plane the endoscope is bending in. The errors in the other directions take both positive and negative

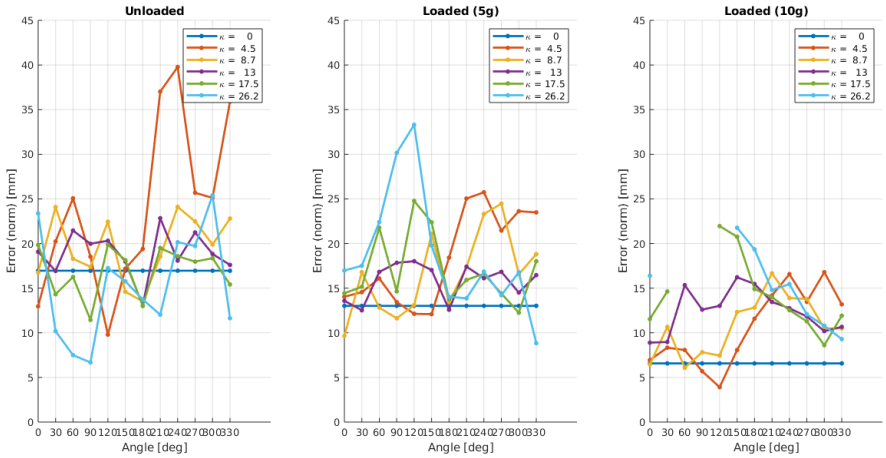

Figure 17: Prediction error per configuration. Different configurations are grouped together per intended radius of curvature (in [1/m]) and plotted over the angle of the bending plane.

values. Most interesting is the behaviour of the error in y-direction (figure 19). When the endoscope is loaded with the largest load (10 grams) the errors follows a clear (inverted) sine-wave trajectory. For the cases with other loads, this trajectory is less clear, but sine-like features can still be observed.

Additionally, with increasing curvature of the endoscope, there seem to be higher prediction errors in the x-direction. The other directions and the magnitude of the total error do not show a clear trend in the plots of figures 17 to 20.

In order to further investigate the errors and observe trends, figures 21 and 22 are presented. These plots show a front view of the endoscope (the yz-plane) and the 2D projections of measured endoscope tip positions in the plane. The error corresponding to a prediction for every tested configuration is represented by a circle whose radius is scaled relative to the magnitude of the error. When no valid prediction could be made the measured point is coloured red and no circle is plotted. Please note that between figures the scaling factor of error radii differs and thus should not be (visually) compared. Subplots in the same figure on the other hand can be directly compared.

The most obvious trend that is observed in the two figures is that with increasing external loads, the prediction error decreases. Exception to this are the six configurations with a 10 grams load, upwards bending (negative z-direction), and high curvature, where the model could not compute a valid prediction (in last plot of figure 22). A similar observation can be made in the case of a 5 grams external load, where the prediction errors for configurations bending upwards are noticeably bigger than those where the endoscope bends down or sideways (from a front-view perspective).

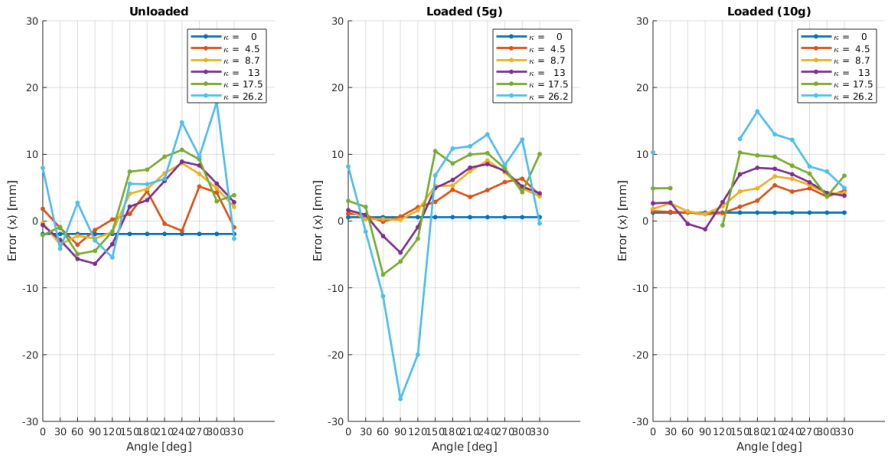

Figure 18: Prediction error in the x-coordinate per configuration. Different configurations are grouped together per intended radius of curvature (in [1/m]) and plotted over the angle of the bending plane.

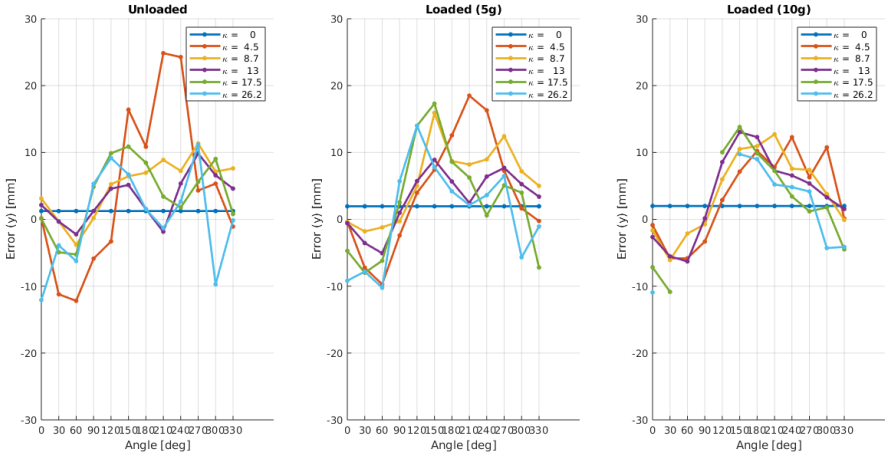

Figure 19: Prediction error in the y-coordinate per configuration. Different configurations are grouped together per intended radius of curvature (in [1/m]) and plotted over the angle of the bending plane.

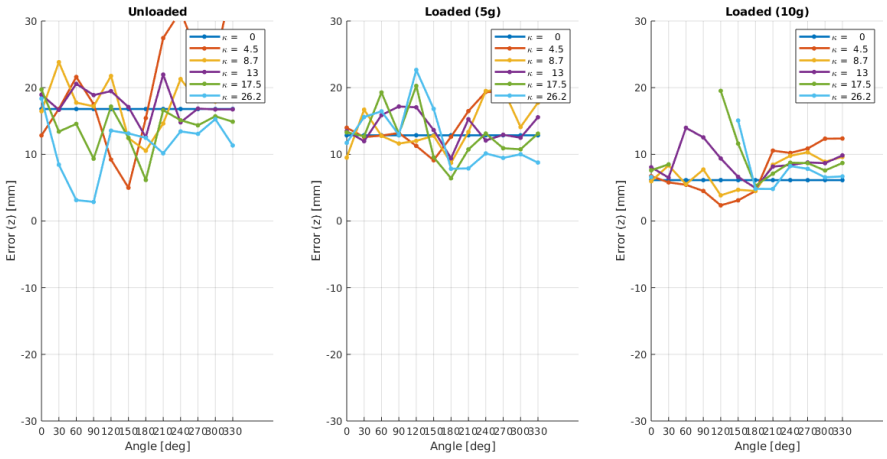

Figure 20: Prediction error in the z-coordinate per configuration. Different configurations are grouped together per intended radius of curvature (in [1/m]) and plotted over the angle of the bending plane.

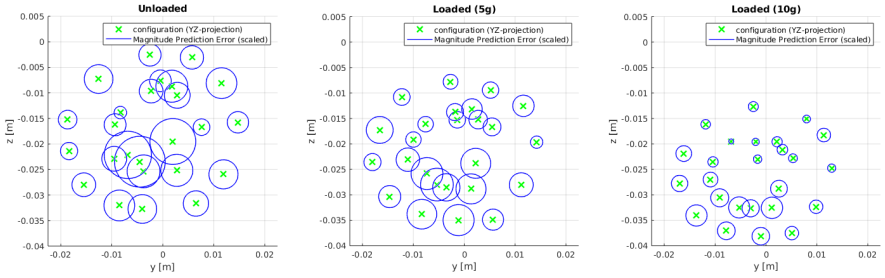

Figure 21: Front view (yz-plane) of the endoscope with measured tip positions marked with crosses. Radii are relative to the scaled down (factor 8) prediction error for every configuration. This figure shows the three smallest radii of curvature (0, 4.5, and 8.7 [1/m]).

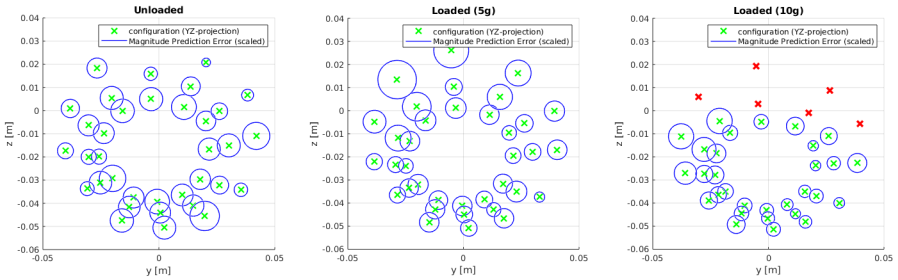

Figure 22: Front view (yz-plane) of the endoscope with measured tip positions marked with crosses. Radii are relative to the scaled down (factor 4) prediction error for every configuration. This figure shows the three largest radii of curvature (13, 17.5, and 26.2 [1/m]).

9.2.1 Additional Predictions

This subsection presents extra predictions that have been done on the previously acquired experimental data. The predictions here use different parameters in order to attempt to provide more insight into the nature of the observed errors. Motivation on which parameters are investigated is presented in the discussion, as it relies on the interpretation of previously described results and observations.

The figures presented here are MATLAB plots that show the root-mean-square (RMS) error of the new predictions with standard deviation (std) upper and lower bounds. Additionally, for every new model evaluation, the number of invalid predictions is shown on a second vertical axis (in red).

The scaling down of tensions, as seen in figure 23, results in better model performance for small reductions in tension, but deteriorates prediction accuracy as the tension gets reduced too much. The number of invalid predictions will generally increase as the tension is reduced, except for the maximally loaded case (10 grams), where there's an optimal minimum near the point where the error is smallest too.

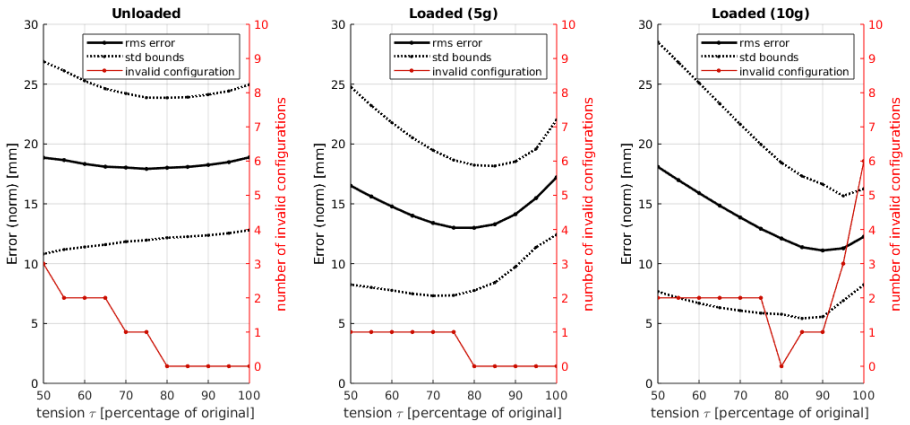

Figure 23: Magnitude of the prediction errors after model revaluation using scaled down values for the tendon tensions, as well as the number of configurations for which a valid solution could not be found.

Figure 24 shows an approximately linear decrease in error as the distributed weight of the endoscope is increased. This decrease in error can be traced back to the error in the (vertical) z-coordinate which exhibits the same behaviour. For the heavily loaded configurations, the decrease is relatively insignificant, and the RMS error stays more or less constant. While there are only valid predictions for the first two loading options (unloaded and 5 grams), the number of invalid predictions for the third option (10 grams) decreases with increased endoscope weight.

When the external tip load is increased — see figure 25 — for the first loaded case (5 grams) it shows a near linear decrease in error. For the second loaded

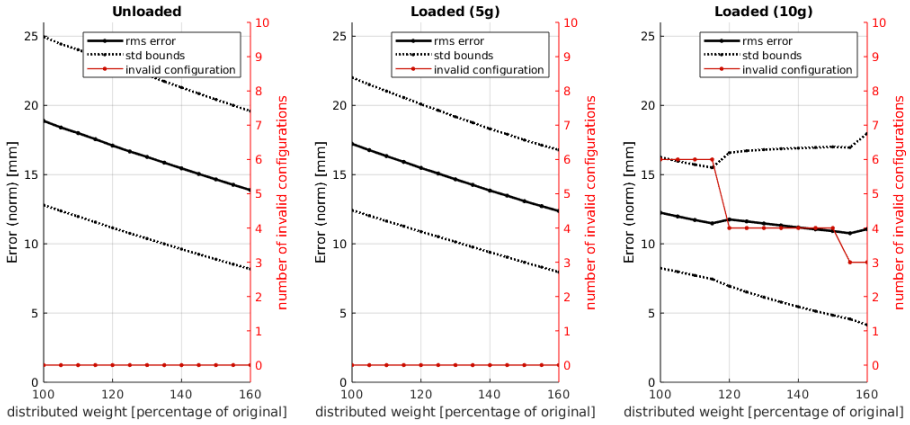

Figure 24: Magnitude of the prediction errors after model revaluation using scaled up values for the endoscope's distributed weight, as well as the number of configurations for which a valid solution could not be found.

case of 10 grams, the error first decreases slightly and then increases again, but shows little change in total. Overall, it shows behaviour similar to an increase in endoscope weight.

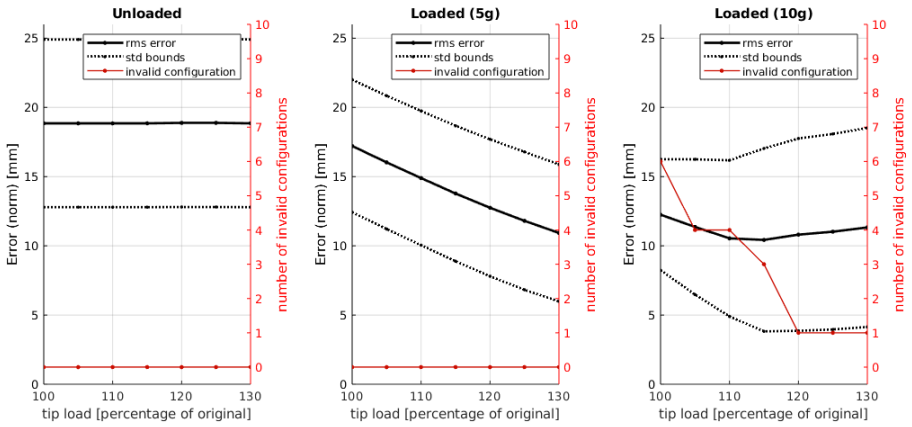

Figure 25: Magnitude of the prediction errors after model revaluation using scaled up values for the external tip load, as well as the number of configurations for which a valid solution could not be found.

10 Discussion

In this section, the results and observations of the experiments are interpreted. From the interpretation a hypothesized explanation for any observed errors or unexpected results can follow. After the interpretation of results, some more general remarks on suspected sources of inaccuracies or errors are made and any observed limitations are discussed. Finally, in its own subsection, some recommendations on future work are presented.

10.1 Interpretation of Results

The individual errors in the stiffness characterization experiment are all between 1 and 2.5 mm in magnitude. On their own these prediction errors seem to be fairly accurate, and thus the resulting optimal stiffness is expected to be accurate as well.

A first observation in the results of the prediction experiment was the fact that the error in the z-direction only took positive values. This leads to believe the model does not accurately take into account the weight of the endoscope. Without changing the implementation of gravitational pull in the model, these errors should then originate from either a faulty stiffness or weight distribution of the endoscope. The former is assumed not to be the main source of error in this case due to the accurate results in the stiffness characterization experiment. Therefore the influence of the latter is investigated. It is already known that the weight distribution along the endoscope is not very accurate due to the assumption that it has a constant cross-section along its backbone (i.e. the spacer discs are not discretized at an interval along the backbone). To implement this, however, would pose a large computational burden on the model. For this

reason, a simplified modification is tested; where the experimental data is re-evaluated using an increased weight of the endoscope (which is still assumed to be evenly distributed).

Additionally, it was observed that with increased external loads the prediction error decreases. When looking at the individual errors per axis, it becomes apparent that an external point load facing downwards helps decrease the error in the z-direction, but not the others. Since there is only a noticeable change in error in the z-direction, this is interpreted as a motivation for re-evaluating the model with an increased tip load.

Furthermore, the typical sine-wave trajectory of the y-error gives some extra insights. To reiterate, in a front-view of the endoscope in the experimental setup, the positive y-axis is horizontal and points to the right. A point on the positive y-axis therefore has a bending plane angle of 0 degrees (with positive angles going towards the positive z-axis, or straight upwards). The prediction error in the y-direction starts off becoming negative for small bending plane angles (approximately between -30 and 90 degrees), corresponding to an endoscope bending to the right (from a front-view perspective) with a prediction that is — horizontally speaking — closer to the origin. Similarly, the error becomes positive in a range of angles between 120 and 240 degrees, which again corresponds to a prediction closer to the origin than the actual measured data.

Most striking, however, is the big discrepancy between the overall results of the stiffness characterization experiment and the prediction experiment. Errors in the latter experiment are easily 10 times as large in magnitude. This leads to the realization that the tendons may not be appropriately modelled, because the main difference between the two experimental setups is that in the latter (the 'main' prediction experiment) the effect of tendon tension is added. Experimental investigation of the effect of adding tensioned tendons cannot be performed due to the unforeseen circumstances. However, this does motivate the urge to re-attempt prediction using different tensions. In order to make a simplified attempt at incorporating tendon-friction, the tensions in the tendons are multiplied by a constant factor (smaller than 1) which scales everything down (i.e. a portion of the measured tension is in fact a frictional force thus the actual tension acting on the endoscope should be lower).

Linearly reducing tension in the tendons by taking only a fraction of each tendon's tension has led to a polynomial error curve with a minimum that approximately matches with an optimum for the number of valid predictions that are computed. The results suggest that friction in the tendons plays a role in the inaccurate predictions that were made. This is supported by the polynomial shape of the error in the revaluation plots (figure 23), which shows that the tension should not be mindlessly reduced. Since this implementation of tendon friction by taking blind fractions of all values is a simplification of reality, it is expected that a more intricate implementation of friction may provide better results.

The similarities between the errors for revaluation with increased endoscope weight and external tip load is not surprising, as both add forces that are directed towards the same direction (gravitational pull). For configurations where

the endoscope is already experiencing significant pull downwards (10 grams external loading), increasing gravitational pull — whether it be by the distributed weight of the endoscope or a point force at the tip — will hardly show any effect in the RMS error anymore. This leads to the realization that the error does not stem from these sources, and revaluation with increased endoscope weight and tip load are only targeting symptoms while ignoring underlying issues.

The external loads are assumed to be exact in direction and position, while in reality as the endoscope bends, this will not be the reality. The mass that hangs from the tip may push against spacers discs in some configurations and the actual loads are likely composed of a small point moment together with a point force that is slightly lower in magnitude than is expected. Yet it's assumed that this is not the most relevant source of errors.

Model evaluations are done with an endoscope that is suspected to be suboptimal and does not comply with all assumptions. The most worrisome assumption was the frictionless contact between tendon and spacer disc. In hindsight the relatively rough surface and edges of the 3D printed polymer may have caused significant friction in the tendons which in turn throws off the model's predictions.

While no quantified evaluation of the actuation system's performance could be conducted, some limitations have been identified. Due to bad scaling between the endoscope's kinematics and DC motor actuation in terms of sensitivity, fine movement of the endoscope is not possible. While the PID controllers that steer the DC motors based on tendon length have sub-millimeter precision, the endoscope is (visibly) sensitive to smaller changes in tendon length.

As the system is actuated and tendons are wound and unwound on the axes, some slack may appear in the tendons. This causes some issues in keeping a constant 'reference' tension in the tendons that would be seen in a neutral configuration. Issues with keeping the tendons tensioned are likely caused by the long paths that the tendons have to travel which introduces play, and tendons that are initially being wound on the actuation axis in a suboptimal manner. When the tendon would later be wound on the axis again but more tightly, this results in less tendon length being retracted and so decreasing tension.

Finally, an issue with having two antagonistic PID controllers working at the same time is addressed. When one tendon is elongated, the opposite tendon is shortened by the corresponding motor pulling on the tendon. When control of the latter tendon overshoots, or the tendon is wound up in an unideal manner that decreases the latter tendon's relative length, another motor will pull on the first tendon to overcome the additional extension that is caused by the overshoot. This results in the two antagonistic motors pulling against one another. While small disturbances of such nature might be overcome by slack in the tendons that acts as a buffer for overshoots, this phenomenon could cause instabilities in the positional PID control of the tendons, especially with the use of integral terms which accumulate the error and cause the motors to only pull more.

10.2 Future Research

Future prototypes of the actuation system are recommended to emphasise scaling-down the setup. By finding an alternative for the tendon-coupling mechanism, a lot of space is opened up in the current design. Additionally, actuation using bulky DC motors is not necessary as the flexible endoscope requires only little power. Alternative methods of tendon-actuation are an interesting viewpoint for reduction of size in new developments concerning this system.

The low-level control of tendons is also recommended to be changed from position to tension control. This would eliminate the aforementioned issues with two antagonistic controllers pulling against each other, while simultaneously opening up a door towards control directly based on the coupled Cosserat Rod-Tendon model's inputs (which include the tendons' tension). It should be noted that this excludes the option of scaling down the actuation hardware by switching to mechanically coupled actuation of two antagonistic tendons by a single motor.

For specifically continuing with a Cosserat based model, research should firstly focus on the influence of adding tendons and if these are properly modelled. As has been illustrated by the additional model evaluations using a very simple implementation of tendon friction, this could be beneficial, however a better implementation should be found.

For more general research in this direction, it might be worthwhile to look at other modelling options, as the results that have been obtained are not accurate enough to outweigh the disadvantage of the complex computation. Especially when friction needs to be included in the model, it is likely to become too complex. It could also be beneficial to spend more effort in endoscope (re)design or the manufacturing process in order to achieve a physical setup that has so little friction it can actually be ignored.

11 Conclusion

With the experiments that have been performed, the results and their interpretations help to form a conclusion on the thesis. Reflecting back on the aim of the thesis, it can be concluded that the project partially succeeded, while leaving a few important caveats.

Specifically on the design part, it has been found that the system that has been developed is capable of actuation a single segment tendon-driven flexible manipulator in two rotational degrees of freedom. The robotic control has been successfully implemented, but complex deformation compensation control has not been achieved in the practical setup. While such a control scheme was not experimentally validated, it is assumed that the corresponding design requirements are sufficiently realized to be capable of handling such control. However, it is recommended that the switch to tension-based control is made.

The prediction and compensation of endoscope deformation has not been realized to a satisfactory extent. While prediction using the coupled Cosserat-

rod model was possible, the prediction errors (order of) were too large to provide any useful input for model-based compensation control. The latter (model-based compensation control) has therefore not been attempted.

All in all, the system that has been designed shows promising functionality for endoscopic control with compensation of deformation due to external loads, however, the algorithm providing control based on predictions requires more work specifically on the modelling of tendon actuation in the endoscope.

Bibliography

[1] S. Begum, H. J. Hansen, and K. Papagiannopoulos, "Vats anatomic lung resections—the european experience," *Journal of thoracic disease*, vol. 6, no. Suppl 2, p. S203, 2014.

[2] O. Onugha, R. Ivey, and R. McKenna, "Novel techniques and approaches to minimally invasive thoracic surgery." *Surgical technology international*, vol. 30, pp. 231–235, 2017.

[3] J. L. Ochsner, "Minimally invasive surgical procedures," *The Ochsner Journal*, vol. 2, no. 3, p. 135, 2000.

[4] G. S. de Mello Granata, "A hundred years of knee arthroscopy," *Revista Brasileira de Ortopedia (English Edition)*, vol. 47, no. 6, p. 684, 2012. [Online]. Available: http://www.sciencedirect.com/science/article/pii/S2255497115300227

[5] J. Burgner-Kahrs, D. C. Rucker, and H. Choset, "Continuum robots for medical applications: A survey," *IEEE Transactions on Robotics*, vol. 31, no. 6, pp. 1261–1280, 2015.

[6] J. H. Medicine. Minimally invasive surgery. [Online]. Available: https://www.hopkinsmedicine.org/minimally_invasive_robotic_surgery/

[7] M. Kanzaki, "Current status of robot-assisted thoracoscopic surgery for lung cancer," *Surgery today*, pp. 1–8, 2019.

[8] K. Xu and N. Simaan, "An investigation of the intrinsic force sensing capabilities of continuum robots," *IEEE Transactions on Robotics*, vol. 24, no. 3, pp. 576–587, 2008.

[9] F. Khan, R. J. Roesthuis, and S. Misra, "Force sensing in continuum manipulators using fiber bragg grating sensors," in *2017 IEEE/RSJ International Conference on Intelligent Robots and Systems (IROS)*. IEEE, 2017, pp. 2531–2536.

[10] J. Feiling, Z. Li, H. Yu, and H. Ren, "Optimal teleoperation control of a constrained tendon-driven serpentine manipulator," in *2015 IEEE 28th Canadian Conference on Electrical and Computer Engineering (CCECE)*. IEEE, 2015, pp. 418–423.

[11] M. Li, R. Kang, S. Geng, and E. Guglielmino, "Design and control of a tendon-driven continuum robot," *Transactions of the Institute of Measurement and Control*, vol. 40, no. 11, pp. 3263–3272, 2018.

[12] P. Berthet-Rayne, G. Gras, K. Leibrandt, P. Wisanuvej, A. Schmitz, C. A. Seneci, and G.-Z. Yang, "The i 2 snake robotic platform for endoscopic surgery," *Annals of biomedical engineering*, vol. 46, no. 10, pp. 1663–1675, 2018.

[13] Z. Li, L. Wu, H. Ren, and H. Yu, "Kinematic comparison of surgical tendon-driven manipulators and concentric tube manipulators," *Mechanism and machine theory*, vol. 107, pp. 148–165, 2017.

[14] R. J. Webster III and B. A. Jones, "Design and kinematic modeling of constant curvature continuum robots: A review," *The International Journal of Robotics Research*, vol. 29, no. 13, pp. 1661–1683, 2010.

[15] J. Starke, E. Amanov, M. T. Chikhaoui, and J. Burgner-Kahrs, "On the merits of helical tendon routing in continuum robots," in *2017 IEEE/RSJ International Conference on Intelligent Robots and Systems (IROS)*. IEEE, 2017, pp. 6470–6476.

[16] K. Oliver-Butler, J. Till, and C. Rucker, "Continuum robot stiffness under external loads and prescribed tendon displacements," *IEEE Transactions on Robotics*, vol. 35, no. 2, pp. 403–419, 2019.

[17] T. Mahl, A. Hildebrandt, and O. Sawodny, "A variable curvature continuum kinematics for kinematic control of the bionic handling assistant," *IEEE transactions on robotics*, vol. 30, no. 4, pp. 935–949, 2014.

[18] G. S. Chirikjian and J. W. Burdick, "A modal approach to hyper-redundant manipulator kinematics," *IEEE Transactions on Robotics and Automation*, vol. 10, no. 3, pp. 343–354, 1994.

[19] M. T. Chikhaoui, S. Lilge, S. Kleinschmidt, and J. Burgner-Kahrs, "Comparison of modeling approaches for a tendon actuated continuum robot with three extensible segments," *IEEE Robotics and Automation Letters*, vol. 4, no. 2, pp. 989–996, 2019.

[20] D. C. Rucker, *The mechanics of continuum robots: model-based sensing and control*. Vanderbilt University, 2011.

[21] F. Qi, F. Ju, D. Bai, Y. Wang, and B. Chen, "Motion modelling and error compensation of a cable-driven continuum robot for applications to minimally invasive surgery," *The International Journal of Medical Robotics and Computer Assisted Surgery*, vol. 14, no. 6, p. e1932, 2018.

[22] R. J. Roesthuis and S. Misra, "Steering of multisegment continuum manipulators using rigid-link modeling and fbg-based shape sensing," *IEEE transactions on robotics*, vol. 32, no. 2, pp. 372–382, 2016.

[23] H. Altenbach and V. A. Eremeyev, *Generalized Continua-from the Theory to Engineering Applications*. Springer, 2012, vol. 541.

[24] K. Xu and N. Simaan, "Intrinsic wrench estimation and its performance index for multisegment continuum robots," *IEEE Transactions on Robotics*, vol. 26, no. 3, pp. 555–561, 2010.

[25] D. C. Rucker and R. J. Webster, "Deflection-based force sensing for continuum robots: A probabilistic approach," in *2011 IEEE/RSJ International Conference on Intelligent Robots and Systems*. IEEE, 2011, pp. 3764–3769.

[26] M. Kouh Soltani, S. Khanmohammadi, and F. Ghalichi, "A three-dimensional shape-based force and stiffness-sensing platform for tendon-driven catheters," *Sensors*, vol. 16, no. 7, p. 990, 2016.

[27] J. Back, L. Lindenroth, K. Rhode, and H. Liu, "Three dimensional force estimation for steerable catheters through bi-point tracking," *Sensors and Actuators A: Physical*, vol. 279, pp. 404–415, 2018.

Appendices

A Force Sensing

Flexible endoscopes in their clinical application are surrounded by a patient's internal organs. Safe navigation within this surrounding which cannot always be fully visualized will depend on the integration of haptic feedback into a control scheme, as was previously mentioned. In order to implement a type of haptic feedback where environmental forces of a remotely controlled manipulator are transferred to a person (typically this would be a surgeon or clinician) operating the remote controller, the external forces that the manipulator is subjected to should be known. The manipulator's shape is influenced by external forces and moments all along its central backbone, but for some applications it may be enough to only measure forces that are experienced at the endoscope's tip.

A simple solution would be to integrate commercially widely available strain-gauge-based sensors into endoscope design. The desired endoscope down-scalability however does not benefit from such solutions, nor does the cost when the endoscope's application requires it to be disposable. For these reasons, there have been some more elegant force measuring approaches proposed in the literature which will be elaborated on below.

Force sensing using joint-level information such as tendon length and tension is commonly referred to as *intrinsic force sensing*. This approach has been a major interest for research, starting with a paper by Xu and Simaan [8] in 2008. This paper presents a wrench sensing algorithm for a single-segment manipulator based on a virtual work model. Measurable wrenches[10] are shown to be limited to two dimensions in the single-segment case when the virtual work model that is described in this paper is used. To overcome the limited dimensionality of sensible wrenches, a wrench measurement is constrained in such a way that four dimensions are null, reducing the underdetermined system to a solvable set of equations. These constraints are defined specific to a clinical application such as palpation, incision, or suture penetration. In 2010 an extension on this approach was published [24]. Here, the previous approach is generalised for multimodule manipulators. A derivation and implementation is shown for a three-segment manipulator, which is validated using simulation and experimental evaluation. The wrench at the tip could now be measured in its full six dimensions due to the serial coupling of three segments each providing two sensible degrees of freedom.

A probabilistic approach is presented by Rucker and Webster [25] in 2011. In this paper, a Cosserat Rod model for a two-segment manipulator is simplified (planar motion/deflection and neglects transverse shear and axial extension). Two-dimensional planar forces at the tip can be measured using an extended Kalman filter (EKF). Such a filter will give optimal estimations by combining

[10] in screw theory a wrench is the dual of a twist and can be considered to be the six-dimensional set of forces (three dimensions) and moments (three dimensions) that an arbitrary point can be subjected to

predictions made by a system model and uncertain measurements. The forces were estimated using the end-effector pose and actuator values (which were defined to be the point torques that the tendons exert on the central backbone at their termination points).

In 2016, Kouh Soltani et al. [26] presented a paper using a similar approach for measuring tri-axial forces at the tip (thus including non-planar loads). Using a simplified Cosserat Rod model, the Kirchhoff Rod model, and modelling tendon actuation as point torques, a single-segment tendon-actuated catheter could measure forces up to 0.4N at its tip. The measured force estimation used a Kalman-filter-based approach which uses curvature and position estimates as measurements. These estimates followed from the MRI images which were assumed to be readily available in the catheter's clinical application which is ablation. This limits the general applicability of the approach, since curvature and position estimations may not always be obtained in such a straightforward way.

Back et al. [27] presented a method for estimating contact forces anywhere along a single-segment catheter's steerable section. This is done by tracking the flexible section's base and tip position in space and comparing the latter to a predicted tip position. The prediction is formed by subsequently applying two deflection models of which the first is based on only the forces applied by tendon tension and the second includes the external contact force. By comparing the tracked and predicted tip position and assuming the resulting difference vector is proportional to the magnitude of the contact force, and additionally assuming another linear relation[11], the contact force can be estimated. For this approach, the contact force's position along the endoscope's backbone should be known, and the tip position should be tracked. For the latter issue, it is suggested to use fluoroscopy imaging or 3D electroanatomical mapping systems. In the experimental validation it seems that only forces at the tip are estimated with the rest of the catheter either unconstrained or physically constrained at a known point along the body.

Khan et al. [9] (from the same group as in [22]) published a paper (2017) in which they used strain measurements from FBG sensors along the manipulator's central backbone to estimate external forces at the tip. Force estimation was done according to two different models: a rigid-link model and a simple Cosserat Rod model. Both models have been experimentally validated and compared with a single-segment manipulator with three fibres each with 8 embedded FBG sensors equally spaced along the central backbone. External forces were applied to the tip under three (perpendicular) angles that presumably have to be interpreted to be axial loads, although this does not become clear. There is no further mention of any force estimations performed under heavy deformation of the manipulator. Using FBG sensors should not be considered an intrinsic type of force sensing since these fibres are independent sensors that are integrated into the manipulator design. However, due to the very small diameter of these fibres this approach does not suffer from down-scalability issues, and their ro-

[11] please refer to the cited paper for a more detailed description of the algorithm

bustness allows for fairly easy chemical sterilization should that be required. On the other hand, a dedicated FBG interrogator is required to translate changes in wavelength to strains (and optionally temperature changes). These pieces of hardware are typically very expensive, causing this form of fibre-optic force sensing to have a big financial overhead.